

**Department of Materials Science
and Technology
University of Crete**



Highly active catalysts (Pt, Cu, Ni) supported on MTiO_3 for hydrogen evolution

Anna Panagiota Souri

Heraklion, December 2022



Ενεργοί Καταλύτες (Pt, Cu, Ni) πάνω σε MTiO₃ για παραγωγή υδρογόνου

Άννα Παναγιώτα Σουρή

Ηράκλειο, Δεκεμβριος 2022

Master thesis Committee:

G. Armatas (Supervisor)

Professor, Dept. of Materials Science and Technology, University of
Crete

I. Remediakis

Associate Professor, Dept. of Materials Science and Technology,
University of Crete

C. Stoumpos

Associate Professor, Dept. of Materials Science and Technology,
University of Crete

SUPERVISING

Dr. Vassilios D. Binas

Visiting Professor, Department of Physics, University of Crete and
Associate Researcher, Institute of Electronic Structure and Laser,
Foundation for Research and Technology- Hellas

Contents

Acknowledgments	6
Abstract	7
Chapter 1 – Introduction	8
1.1 Solar Hydrogen Evolution	8
1.1.1 Principles in heterogeneous photocatalysis	9
1.1.2 Thermodynamics for water splitting.....	10
1.1.3 Quantum yield	13
1.2 Photocatalysts for H ₂ production	16
1.2.1 Metal Titanates.....	16
1.2.2. Strontium titanate SrTiO ₃	18
1.2.3 Calcium titanate CaTiO ₃	20
1.3 Cocatalysts	21
1.3.1 Photodeposition of cocatalysts	24
1.4 Master Thesis objective	28
Chapter 2 – Experimental Section	29
2.1 Synthesis of metal titanates	29
2.1.1 Synthesis of STO and CTO	29
2.2 Photodeposition of metals supported on metal titanates.....	29
2.2.1 Photodeposition of Pt nanoparticles on STO.....	29
2.2.2 Photodeposition of Ni and Cu nanoparticles on STO	30
2.3 Structural, morphological and optical properties	30
2.3.1 X-ray diffraction (XRD).....	30
2.3.2 Scanning electron microscopy (SEM) and energy dispersive X-ray spectroscopy (EDX).....	30
2.3.3 Transmission electron microscopy (TEM)	30
2.3.4 Ultraviolet–visible spectroscopy (UV-Vis)	30
2.3.5 Impedance spectroscopy	31
2.3.6 Photoluminescence (PL)	32
2.3.7 Photocatalytic experiments for H ₂ evolution	32
Chapter 3 Results and discussion	33
3.1 Characterization of metal titanates	33
3.1.1 Structural characterization.....	33
3.1.2. Morphological characterization	34
3.1.3. Optical characterization	35
3.2 Active catalysts (Pt, Cu, Ni) supported on STO	36

3.2.1 Pt catalysts supported on STO	37
3.2.1.1. Structural properties.....	37
3.2.1.2 Morphological properties	38
3.2.1.3 Optical properties	39
3.2.2 Ni catalysts supported on STO	41
3.2.2.1 Structural properties.....	41
3.2.2.2 Optical properties	43
.....Error! Bookmark not defined.	
3.3.3 Cu catalyst supported on STO	44
3.3.3.1 Structural properties.....	44
3.3.3.2 Optical properties	45
3.5 Photocatalytic results	46
3.5.1 Hydrogen evolution of metal catalysts supported on STO	46
3.5.1.1 Hydrogen evolution of Pt supported on STO	46
3.5.1.1.1 Photocatalytic Mechanism towards H ₂ production of Pt supported on STO	47
3.5.1.2 Hydrogen evolution of Ni supported on STO	50
3.5.1.3. Hydrogen evolution of Cu supported on STO	51
3.5.2. Stability	53
Chapter 4. Conclusions and perspectives	56
Chapter 5. References.....	57

Acknowledgments

I would like to thank my supervisor Dr. V. Binas for letting me be part of this group and assigning me this project and for the constant support in every problem and question I ever had.

I would like to thank Prof. G. Armatas, Prof. I. Remediakis and Prof. C. Stoumpos for accepting to be members of my master thesis committee. A special thank you to Prof. G. Armatas and his group for the useful feedback on my thesis. Also, a special thank you to I. Vamvassakis for the help with Mott Schottky measurements and their comprehension.

A big thank you to the whole TCMD group for the wonderful times we had and especially M. Gagaoudakis, M. Moschogiannaki, M. Charalambakis, E. Mantziou, J. Kalofonos, S. Stefa, L. Zouridi and M. Zografaki. A special thank you to L. Skliri for the constant support, helpful feedback and for always finding a solution to every problem I came across.

Finally but definitely not least, thank you to my family and friends close or apart, your support never goes unnoticed!

Abstract

The aim of this master thesis is the synthesis and characterization of highly active catalysts (Pt, Cu, Ni) supported on metal titanates (MTiO_3 , M: Sr, Ca) in order to be used for hydrogen evolution. Most metal titanate materials traditionally are not active photocatalysts for hydrogen evolution as their band positions are not appropriate. However SrTiO_3 (STO) and CaTiO_3 (CTO) differ as the minimum of their conduction band is more negative than the reduction potential of hydrogen. Additionally, the pairing with metal or transition metal-based cocatalysts has been proven to remedy high recombination rates, charge dissociation and transportation and the lack of active sites on the catalyst's surface. Herein, metal titanates STO and CTO were used as support materials for the deposition of highly active metal or transition metal-based cocatalysts like Pt, Ni and Cu. The emphasis thus, is given to the photodeposition of highly active catalysts (Pt, Ni, Cu) supported on STO. Therefore, all the synthesized powders were analyzed by powder X-Ray Diffractometry (XRD), Scanning Electron Microscopy (SEM), Energy Dispersive X-Ray Spectroscopy (EDX), UV-Vis-NIR spectroscopy, Photoluminescence (PL) and impedance spectroscopy. Finally, the powders were tested in photocatalytic water splitting for H_2 production, with the highly active catalysts supported on STO increasing the activity and stability of the individual materials under solar and visible irradiation.

Chapter 1 – Introduction

1.1 Solar Hydrogen Evolution

One of the main challenges humanity has to tackle is the ability to acquire sustainable and clean energy. Issues such as the exponential population growth and the depletion of fossil fuel reservoirs coupled with their environmental impact have shifted the attention towards alternative and renewable energy sources. An energy source capable of meeting these standards is none other than the sun. The solar energy is an endless and environmentally friendly source, which renders photocatalysis an attractive technology for solving the serious environmental and energy – related problems, such as water splitting, CO₂ reduction and water disinfection. Hence, the need to harvest and convert solar energy to fuel has been the subject of intensive research. In an attempt to mimic nature, photocatalytic water splitting for hydrogen production could be part of the solution since it is thought of as artificial photosynthesis. More specifically, the conversion of photon energy to chemical energy, plus the positive change in the Gibbs free energy is a common step in both processes (**Figure 1**).

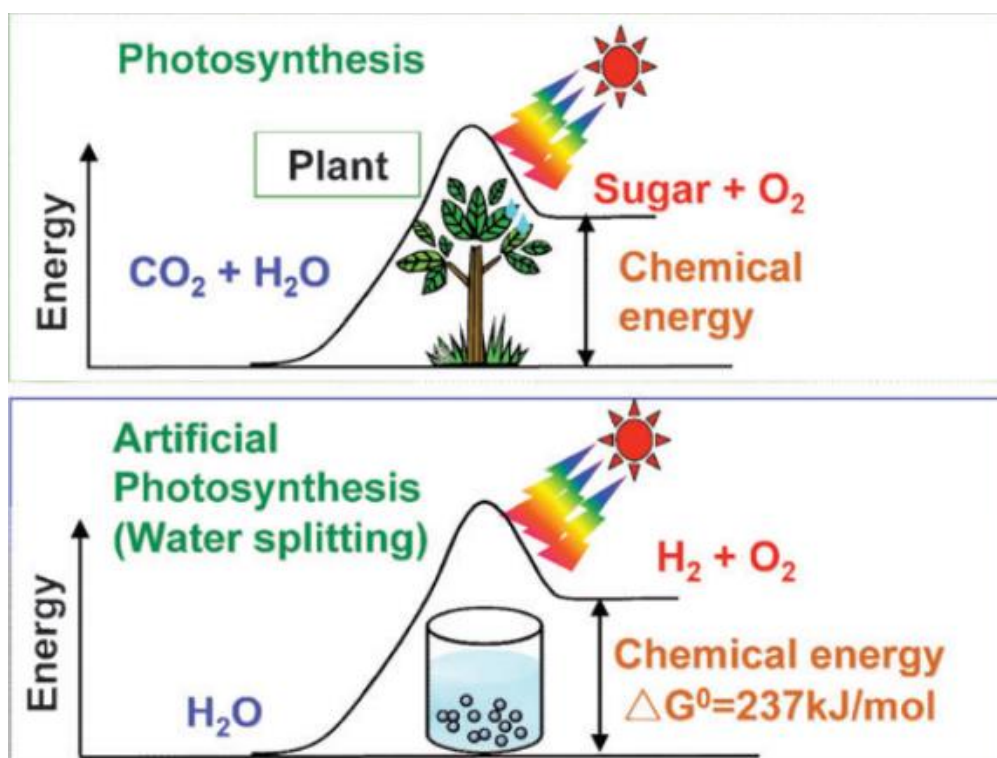


Figure 1: Photosynthesis by green plants and photocatalytic water splitting as an artificial photosynthesis [1]

1.1.1 Principles in heterogeneous photocatalysis

In the heterogeneous photocatalysis of organic and inorganic compounds the interaction of the semiconductor with the incident light is the first step that generates electron-hole pairs. Thus, mobile electron and holes (free excitons) are photogenerated in the CB and VB, creating pathways as seen in **Figure 2**. However, there are two disadvantageous recombination processes that may take place and compromise the photocatalytic activity. These are either the photogenerated charge carriers recombine on the surface of the semiconductor (pathway A) or in the bulk structure (pathway B) in a few nanoseconds. At the same time, photogenerated charges spontaneously migrate to the semiconductor surface and some may further be transferred to organic or inorganic species, or even the solvent's molecules that are pre-adsorbed on the surface. Also, electrons are donated by the semiconductor to reduce an electron acceptor (pathway C) and holes migrating to the surface oxidize an electron donor (pathway D). Hence, anodic and cathodic redox reactions can occur. These constitute the basic principle of semiconductor based photocatalysis for light energy conversion[2].

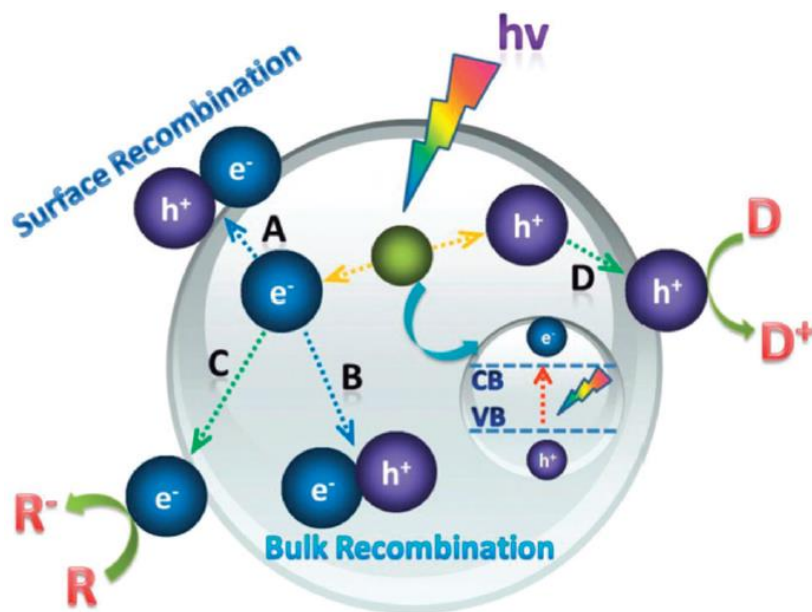


Figure 2: Schematic illustration showing photoexcitation in a semiconductor followed by de-excitation events.[2]

1.1.2 Thermodynamics for water splitting

Water splitting is an uphill endothermic reaction with a high positive change in Gibbs free energy (**equation 5**). In order to split a water molecule in H_2 and O_2 the Gibbs free energy should be positive and equal to $\Delta G = 238 \text{ kJ/mol}$, 2,46eV per molecule. In the case of thermal equilibrium ($\Delta H = \Delta G = 0$) there is no driving force to generate electron-hole pairs. Hence, the reaction energy in photocatalysis is the Gibbs free energy that derives from light activation.

Semiconducting water splitting to obtain H_2 can be summed up in 6 main stages (**Figure 3**). The process initiates with light harvesting, the semiconductor absorbs the incident light (stage 1). Then comes the charge excitation, the formation of electron-hole pairs (stage 2). These pairs need to dissociate and transfer to the material's surface (stages 3, 4) where they participate in catalytic reactions (stages 5, 6). Typically semiconducting photocatalysts have a valence band (VB) and a conduction band (CB) separated by the energy gap (E_g). The incident light must be equal or greater than the E_g in order to activate the semiconductor.

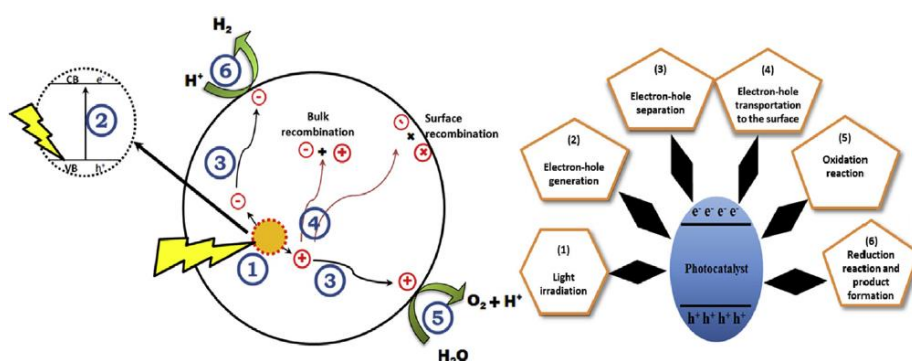
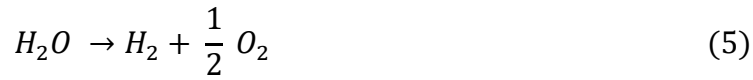
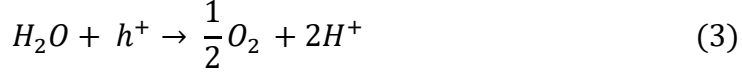
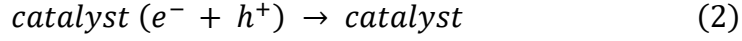
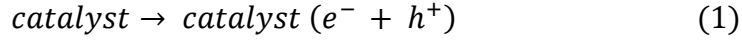


Figure 3: Illustration of mechanism of photocatalytic water splitting for H_2 production[3]

The photogenerated carriers are involved in the reduction and oxidation reactions with water. Moreover, holes oxidize water giving H^+ and electrons reduce H^+ into H_2 (**equations 3** and **4**). It has to be mentioned that redox reactions take place when the reduction and oxidation potentials are above and below CB and VB levels, respectively. Having said that there is also the recombination possibility of charges that releases unproductive heat (**equation 2**) and is considered a great challenge. Inferentially, there is difficulty in achieving H_2 production in pure water in account of fast recombination rate of charge carriers. Thus, sacrificial agents such as methanol, ethanol and glycerol are added to inhibit recombination.



The overall efficiency of a semiconductor hides in three intrinsic characteristics that are, the bandgap, the absolute potentials of E_{CB} and E_{VB} and the dynamics of the created charges such as diffusion length, mobility, lifetime, rate of surface charge recombination and interfacial charge transfer. More analytically, the bandgap dictates which part of the spectrum activates the semiconductor, for instance, semiconductors with $E_g > 3,0$ eV are activated through UV light and thus can take advantage of a small fraction of the solar spectrum, whereas semiconductors with $E_g < 3,0$ eV harvest the solar spectrum more efficiently. Despite that, the minimum bandgap energy that is thermodynamically allowed is 1,23 eV that is the oxidation potential of water in pH=0 (**Figure 4**). Additionally, the knowledge of the band positions or the flat band potentials is an indication of the limitations as far as the photoreactions of the charge carriers are concerned. The position of the bottom of the CM is the reduction potential of the photogenerated electrons and the position of the top of VB reflects the oxidizing ability of photogenerated holes, thus revealing the ability of a system to promote reduction and oxidation. An example of the ideal semiconductor's band positions can be seen in Figure 3 where the bottom of the CB should be more negative than the redox potential of H^+/H_2 (-0,41 eV at pH = 7 or 0 eV at pH = 0) and the top of the VB should be more positive than the redox potential of O_2/H_2O (0,82 eV at pH = 7 or 1,23 eV at pH = 0).

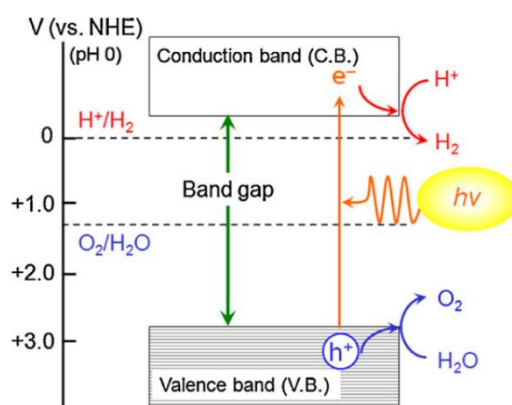


Figure 4: Basic principle of overall water splitting on a semiconductor particle [4]

As already mentioned overall water splitting is harder to be achieved owing to its uphill nature. On the other hand, half reactions are easier to take place if the appropriate semiconductor is used. Other studies indicated that the addition of sacrificial agents or hole scavengers can capture photogenerated holes much faster because they have more negative redox potential than water leading to higher H₂ evolution rate

1.1.3 Quantum yield

As mentioned above the main parts of the water splitting process include photon absorption and exciton generation in a semiconducting photocatalyst, separation-migration of charges and reduction and oxidation surface reactions. A measure to conclude a photocatalyst's efficiency should thus, take into account the efficiencies of all the aforementioned processes. So, the total efficiency should be (**equation 6**)

$$\eta_{total} = \eta_{absorption} \times \eta_{separation} \times \eta_{reaction} \quad (6)$$

where $\eta_{absorption}$ is the photon absorption efficiency due to the excitons that the incident photon flux creates, $\eta_{separation}$ is the charge separation efficiency that corresponds to the charges that manage to reach the surface of the material and participate in the redox reactions and $\eta_{reaction}$ is the efficiency of the surface redox reactions.

The solar energy conversion and the lifetime of a catalyst are used to draw a conclusion about the efficiency. Practically that means the rate of reaction concerning the total gas produced per unit illumination time. Despite the rate of reaction often measured in $\mu\text{moles g}^{-1}\text{h}^{-1}$ it is not comparative to the mass of the catalyst used, and the reaction rates from different experimental settings and conditions cannot be compared to each other. In order to compare the efficiencies of different photocatalysts from different groups independently from experimental conditions and settings the concepts of apparent quantum yield (AQY) (**equation 7**), solar to hydrogen conversion efficiency (STH) (**equation 8**) and turnover frequency (TOF) (**equation 9**) have been emerged.

$$A. Q. Y (\%) = \frac{2 (\text{number of } H_2 \text{ molecules released})}{\text{number of incident photons}} \cdot 100 \quad (7)$$

$$STH (\%) = \frac{\text{energy of generated } H_2}{\text{energy of incident solar light}} \cdot 100 = \frac{E_{H_2}}{E_{solar}} \cdot 100 \quad (8)$$

$$\text{where } E_{H_2} = \left(H_2 \text{ in } \frac{\text{mol}}{\text{sec}} \right) \cdot 232 \frac{\text{kJ}}{\text{mol}} \text{ and } E_{solar} = P \cdot S \cdot t$$

$$P = \text{irradiated solar energy} \left(\frac{W}{m^2} \right),$$

$$S = \text{area of irradiation (m}^2\text{) and } t = \text{irradiation time (sec)}$$

$$TOF = \frac{\text{mol}_{H_2}}{\text{mol}_{cat} \cdot \text{time}} \quad (9)$$

The quantum yield assesses the ability of a photocatalyst for water splitting and is calculated as the number of reacted electrons to the number of absorbed photons. However, this version does not take into account the scattering and reflection of light so the apparent quantum yield (AQY) is recommended, that reflects more frankly how efficiently the incident photons are utilized in an intended photocatalytic reaction. The solar to hydrogen conversion efficiency (STH) is the amount of solar energy stored as hydrogen to the incident solar energy. It reveals the quantity of solar energy that is harvested through water splitting by a photocatalyst[5]. Finally, the turnover frequency (TOF) is the number of water molecules split on an active site in a particular period of time (sec).

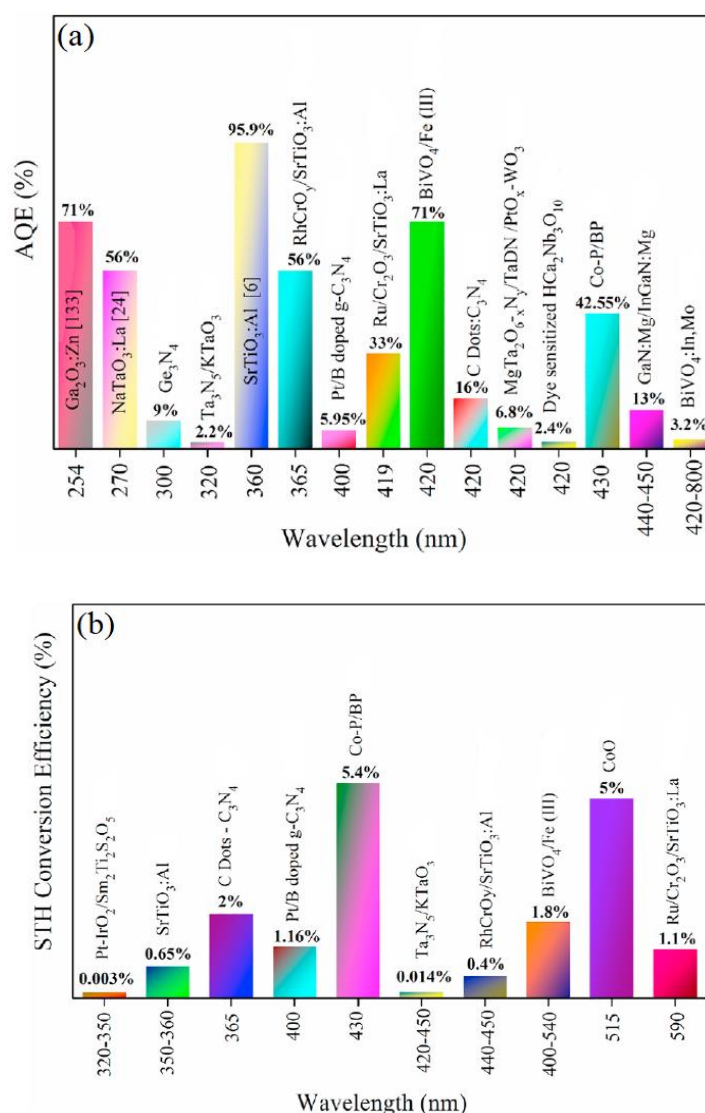


Figure 5: (a) the apparent quantum efficiency of various overall water splitting photocatalysts, (b) the highest reported STH conversion efficiencies of various photocatalysts [6]

In **Figure 5 (a)** different photocatalysts are being compared regarding their AQY and the wavelengths at which they acquire it. Takata et al [7] reported one of the highest AQY with a value of 96% at wavelengths between 350nm and 360nm. The photocatalyst that they used was Al doped SrTiO_3 ($\text{SrTiO}_3\text{:Al}$) loaded by photodeposition process co-catalysts Rh, Cr_2O_3 and CoOOH on various crystal facets. Also, high AQY was reported from Sakata et al [8]. In this case $\text{Ga}_2\text{O}_3\text{:Zn}$ was used as a photocatalyst and reached an AQY of 71% under irradiation of monochromatic light at 254 nm using a top irradiation type cell. In **Figure 5 (b)** different photocatalysts can be seen in association with their STH efficiency and the range of the wavelengths at which they acquire it. Tian et al [9] synthesized amorphous cobalt phosphide (Co-P)-supported black phosphorus nanosheets that could produce hydrogen from pure water without any sacrificial agent, that reached an AQY of 42,55% at 430 nm, and a STH efficiency of 5,4% at 353K. Close to this value Liao et al [10] reported pure CoO nanoparticles that reached a 5% STH efficiency but they were unstable and became deactivated after 1 h of reaction.

1.2 Photocatalysts for H₂ production

As already mentioned a future energy system based on H₂ would solve the fossil fuel depletion issue and the environmental concerns. Despite the fact that H₂ up until now is produced through steam methane reforming it can be produced through water and sunlight. There are three ways to produce H₂ from water, that is electrolysis, thermochemical water splitting and photoelectrolysis / photocatalysis. Since the work of Honda and Fujishima [11] that split water in an electrochemical cell consisted of Pt and TiO₂ electrodes under electric bias, TiO₂ has been widely and meticulously studied for photocatalytic and electrocatalytic water splitting. Although, TiO₂ is considered one of the most studied photocatalysts as it is cheap, non-toxic, readily available and environmentally friendly its photoactivity is quite low. Besides pure phased TiO₂, similar TiO₂-based materials like titanates and other metal oxides have attracted the attention for photocatalytic H₂ generation. For instance, the group of Yuan [12] studied the photocatalytic HER activity of transition metal-doped lepidocrocite-type TiO₂ nanosheets with oxygen vacancies, Yuan et al [12] studied the hydrogen production and electronic properties of single-layered TiO₂ nanosheet modulated by transition metal doping with Cr and biaxial strain. Zhu et al [13] prepared photocatalysts with decorated red phosphorous on TiO₂ nanofibers to investigate the hydrogen generation from pure water. Also, Ou et al [14] paired ultrathin MoS₂ with modified black Ti³⁺-TiO₂ nanotubes via electrospinning-hydrothermal treatment-reduction method and attributed the increase in the H₂ production at the Pt-like behavior of MoS₂ and the presence of Ti³⁺ ions.

1.2.1 Metal Titanates

Complex or mixed oxides can be defined as oxide groups consisting of two or more different cations. An important structure of mixed oxides is perovskite where its typical chemical formula is ABX₃ (A and B denote different cations). Perovskites obtain a crystal structure in which the cations in A and B sites have different sizes ($r_A > r_B$) and X site is an anion (normally O). Metal titanates are perovskite structures where in the chemical formula ABO₃, B is Titanium. These kinds of mixed oxides are used in a wide range of applications due to the variety of structures and properties that they obtain. Particularly, they have attracted the attention in virtue of their potential as photocatalysts for water splitting, their easily tunable bandgap and their photostability and corrosion resistance in aqueous solutions. Despite that their bandgap or band edges do not allow high performance in photocatalytic water splitting, for instance the majority of titanates' bandgaps are above 3eV as seen in **Figure 6**. It has to be mentioned that from all the depicted metal titanates SrTiO₃, MgTiO₃, ZnTiO₃ and CaTiO₃ are capable for HER, while the rest are suitable for OER.

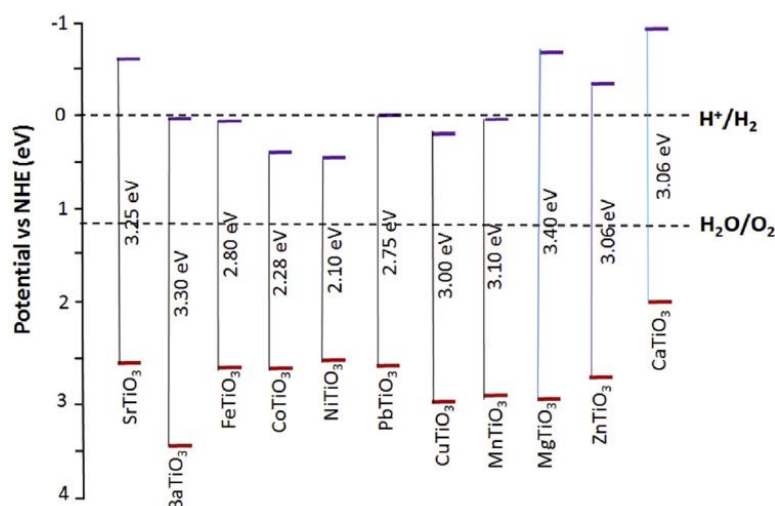


Figure 6: Titanate-based perovskites and their bandgaps and band edges with respect to the redox potential of water splitting [15]

Although CoTiO₃ has a conduction band below the hydrogen reduction potential it has been studied for photocatalytic water splitting for oxygen production. Qu et al [16] synthesized CoTiO₃ nanorods via an ethylene glycol-mediated route and achieved oxygen production yield up to 64.6 mmolh⁻¹ without co-catalysts. Also, Lakhera et al [17] achieved a rate of 600 μmolesg⁻¹h⁻¹ with TiO₂/NiTiO₃ nanocomposite. Paramanik with the Cu_xP/PbTiO₃ type-II p-n junction presented a strategy to improve charge separation and transportation simultaneously for efficient generation of gaseous H₂ under light irradiation[18]. Zhu investigated the photocatalytic activity of metal-free Z-scheme Si/MgTiO₃ heterojunction and reported a production rate of 900 μmol/g generated from sacrificial free, pure water. Another example of classic cubic perovskite, CaTiO₃ doped with Cu on the B-site was studied with density functional theory (DFT) by Zhang for its potential use in photocatalytic HER [5]. Finally, SrTiO₃ is one of the most widely used and studied among metal titanates.

1.2.2. Strontium titanate SrTiO₃

Strontium titanate (STO) is a classic example of cubic perovskite ternary oxide with space group Pm3m and $a=3,9046\text{\AA}$ [19]. Its structure consists of a corner-shared network of TiO₆ octahedral where all interstitial 12-coordinate sites are filled by Sr or from a different view cubic closed-packed layers of SrO₃ with octahedral sites only associated with O nearest neighbors filled by Ti (**Figure 7**). Hence, the atomic sizes of the ion metals are: $\text{Sr}^{2+} > \text{Ti}^{4+}$ [20].

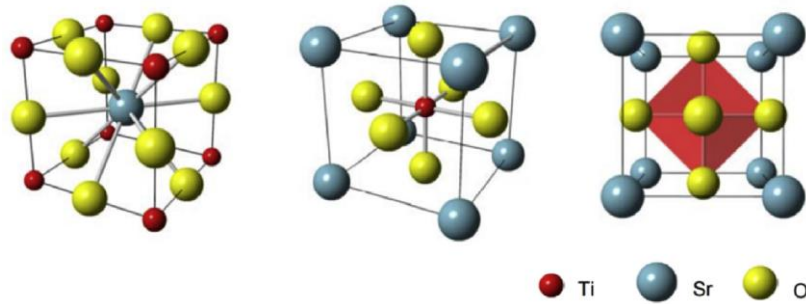


Figure 7: The unit cell structure of SrTiO₃ [20]

STO belongs to the wide bandgap semiconductors ($E_g = 3.1\text{--}3.3\text{ eV}$), so it is activated through ultraviolet light ($\lambda > 380\text{ nm}$), and its density is 5.18 g/cm^3 at ambient temperature. It is n-type semiconductor with indirect band gap and the top of the valence band is mostly formed by the O 2p orbitals, whereas the bottom layers of the conduction band is formed by the Ti 3d orbitals [20] (**Figure 8**).

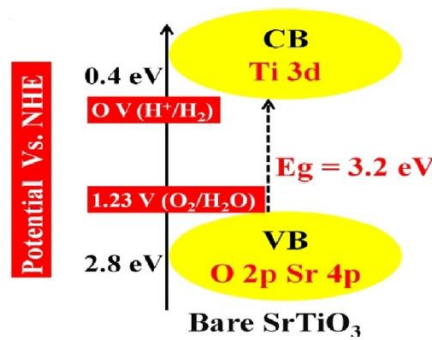


Figure 8: Band gap alignment of SrTiO₃ [19]

The high thermal and chemical stability of STO makes it suitable for various applications. For instance, donor-doped STO has been used in solid oxide fuel cells (SOFC) as anode material[21]–[25], however the pristine STO suffers from low electrical conductivity making it unsuitable for this application. To overcome this, La is introduced as a good dopant because its ionic radius is similar to Sr ($r_{\text{La}^{3+}} = 1.32\text{\AA}$,

$r_{\text{Sr}^{2+}}=1.44\text{\AA}$). Xiaohong Lv et al [26] studied how the simultaneous La-doping and A-site deficiency concentrations affect the electrical conductivity of $(\text{La}_x\text{Sr}_{1-x})_{1-y}\text{TiO}_{3-\delta}$. Moreover, by exploiting the high melting point, the good stability as already mentioned and the ability of STO to detect gas in elevated temperatures it has also found application in sensors, in the form of thin films[27]–[29] or as part of a composite material[30]–[32]. Storage is also an application in which STO has been proved useful, either in hydrogen [33]–[35], energy[36]–[38] or even thermal energy storage[39]. The high Seebeck coefficient that STO possesses makes it a valuable oxide in thermoelectric applications as well. It has been used, doped in A or B site [40], [41] and as a part of a composite paired with graphene oxide [42], [43].

Due to its unique intrinsic properties, STO has been widely employed as a photocatalyst. Whether stemming from its ability to photogenerate charge carriers when irradiated with UV light and the position of its band edges it has been used in photocatalytic degradation of organic pollutants and in photocatalytic hydrogen production. The combination of the overgrown population, the exploitation of nonrenewable fossil fuels and the rapid industrialization has taken a toll on the planet in the form of pollutant accumulation. Hence, a need to degrade these pollutants has appeared that must be tackled, so advanced oxidation processes include the generation of highly reactive species, namely, hydroxyl ($\text{OH}\cdot$) and superoxide radicals ($\text{O}_2^{\cdot-}$) from photocatalysts that oxidize them. Consequently, STO has been studied for photocatalytic dye degradation [44]–[47], Cr (VI) removal [48], [49], phenol degradation and oxidation [50], sulfamethoxazole degradation[51] and degradation of volatile organic compounds (VOC) such as toluene [52], [53].

As far as the water splitting is concerned, STO has been studied doped with or without noble metals. Zong synthesized 1.0%CoP/Al:STO, with evolution rates of 2106 and 1002 $\mu\text{mol h}^{-1} \text{g}^{-1}$ for H_2 and O_2 , respectively [54]. Liu prepared Cr-doped $\text{SrTi}_{1-x}\text{Cr}_x\text{O}_3$ ($x = 0.00, 0.02, 0.05, 0.10$) powders with solvothermal method that increased the photocatalytic activity[55]. Wang [56] synthesized Ce/N co-doped SrTiO_3 that reached a rate of H_2 production of 4.28 $\text{mmol g}^{-1}\text{h}^{-1}$, which is 84.49 times higher than that of pure SrTiO_3 . Also, Al: SrTiO_3 coupled with RhCr_2O_3 and CoOOH cocatalysts and with Au nanoparticles deposition synthesized by Elkodous [57] reached a H_2 evolution rate of 41mmoles /3h. Chiang et al [7] studied Al-doped SrTiO_3 loaded with a rhodium-chromium mixed oxide ($\text{RhCrO}_x/\text{STO:Al}$) for photocatalytic overall water splitting and had an apparent quantum yield (AQY) of 56% under 365 nm ultraviolet (UV) light. Kumar [58] studied the codoping effect on SrTiO_3 of Mn at the Sr site and N at the O site and how it affected the photocatalytic water splitting. Mesoporous STO with Pt deposition was reported to enhance photocatalytic hydrogen production from Tarawipa Puangpetcha et al [59] and Tamiolakis et al [60], with H_2 production rated of 276 and 188 $\mu\text{mol h}^{-1} \text{g}_{\text{cat}}^{-1}$ and 714 μLh^{-1} respectively. Finally, Su et al paired SrTiO_3 , with TiO_2 and Pt and achieved an H_2 rate of 3513 $\mu\text{moles/gh}$ at the optimal Pt loading of 0.5wt% [61]

1.2.3 Calcium titanate CaTiO_3

Calcium titanate CaTiO_3 is the mineral called perovskite after the Russian mineralogist, Count Lev Alexevich Von Perovsk who discovered it. Although it is a classic example of cubic structure, its structure varies with temperature. Based upon the temperature changes it exists in four space groups: cubic ($\text{Pm}\bar{3}\text{m}$), orthorhombic (Pbnm), orthorhombic (Cmcm), tetragonal (I4/mcm). Among these phases the most stable phase is the orthorhombic phase (Pbnm). At temperatures below 1380 K, it exhibits an orthorhombic symmetry with space group Pbnm . Between 1380 and 1500 K, it undergoes a phase transition to a tetragonal structure and above 1500 K, it has a tetragonal symmetry with a space group I4/mcm . Finally, for temperatures above 1580 K, CaTiO_3 exhibits a cubic structure with a space group $\text{Pm}\bar{3}\text{m}$. It is a ternary oxide that has received extensive attention in recent years, due to its unique structural features, high chemical stability, optimum band edge positions, strong catalytic activity, inexpensiveness, low toxicity and easy synthesis.

As already mentioned owing to its appropriate conduction and valence band positions it has been studied for water splitting. For instance Dai[62] modified CTO nanocubes with ZnIn_2S_4 to study its photocatalytic water splitting ability for H_2 production. Wang et al [63] synthesized hollow CaTiO_3 cubes co-doped with La and Cr for HER and reported an apparent quantum efficiency $\sim 2.41\%$. Lu [64] coupled CTO with Cu nanoparticles and achieved a hydrogen evolution rate of $251 \mu\text{mol g}^{-1} \text{h}^{-1}$. Also, Pei et al [65] reported a visible-light active CTO photocatalyst with a hierarchical architecture constructed from single crystal nanowires, prepared by a one-pot hydrothermal reaction using polyvinyl alcohol (PVA) as structure directing agent that reached a H_2 production of $90 \mu\text{moles g}^{-1}$ under 2 hours of irradiation. Cai [66] reported efficient disorder-engineered CTO nanosheets photocatalysts that reached $115 \mu\text{moles}$ of H_2 production under 2.5 hours of irradiation. Finally, Soltani [67] studied the effect of transition metal oxide cocatalyst on Ag loaded CTO as far as photocatalytic H_2 is concerned and discovered that FeO_x/CTO had $500 \mu\text{moles}$ H_2 production under 2 hours of irradiation.

1.3 Cocatalysts

Most photocatalytic systems for H₂ production suffer from disadvantages that include insufficient number of active sites on their surface and high recombination rates of charge carriers. Co-catalysts loaded on the surface of semiconductors promote the separation and migration electron-holes pairs and provide active sites for photocatalytic H₂ production, in contrast to single-component photocatalysts. Therefore, the loading of co-catalysts has been proven to remedy these disadvantages as they play roles of paramount significance (**Figure 9**).

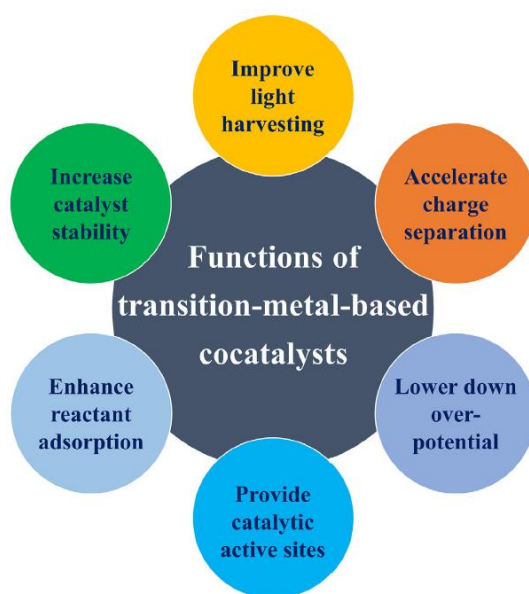


Figure 9: Functions of transition-metal-based co-catalysts in photocatalytic water splitting[68] .

Up until now, the majority of cocatalysts used and studied are noble-metal concentrated, for instance, pure noble metals or even their oxides. Regrettably, the scarcity, inability for large scale applications and their high cost as well, has created a need for other cocatalysts. Transition metal-based cocatalysts obtain compelling virtues as they are easier to find and inexpensive. Judging from their role in photocatalytic water splitting and the type of charge-carriers they trap they can be separated in two groups, the reduction cocatalysts because they trap electrons for HER and the oxidation cocatalysts as they trap holes for OER.

As mentioned earlier it is very beneficial to exploit the visible region of the electromagnetic spectrum as the UV region is only a small fraction of the whole solar spectrum (it corresponds only to a 3–4% fraction of the solar spectrum). Metallic or transition metal-based co-catalysts can improve the harvesting of visible. Moreover, when a metal cocatalyst is loaded on the surface of a semiconductor, if the frequency of the incident photons matches well with the inherent frequency of the metal's free electrons, collective oscillations take place and the metal particles absorb strongly the

photon energy (**Figure 10**). Also, co-catalysts enhance interfacial separation and transfer of photogenerated charges between photocatalysts and cocatalysts preventing their recombination. These abilities in combination with the formation of interfacial interactions result in the aggregation of electrons to the reduction cocatalysts in order to reduce H^+ to H_2 or, on the contrary to the aggregation of holes to the oxidation cocatalysts to oxidize water to O_2 .

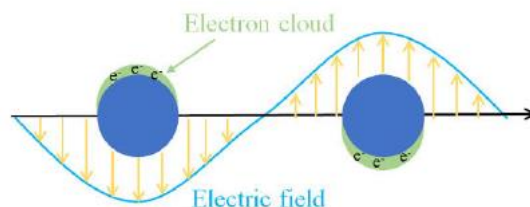


Figure 10: Schematic of LSPR effect [69]

Other ways co-catalysts advantageously affect these photocatalytic systems is through the minimization of the overpotential of surface redox reactions and the creation of adequate active sites. Finally, stability is also an issue that is positively affected by co-catalysts. For instance, some metal sulfides oxidize easily, when paired with co-catalysts self-decomposition of sulfides is inhibited by extracting the photogenerated holes for oxygen evolution reactions[70].

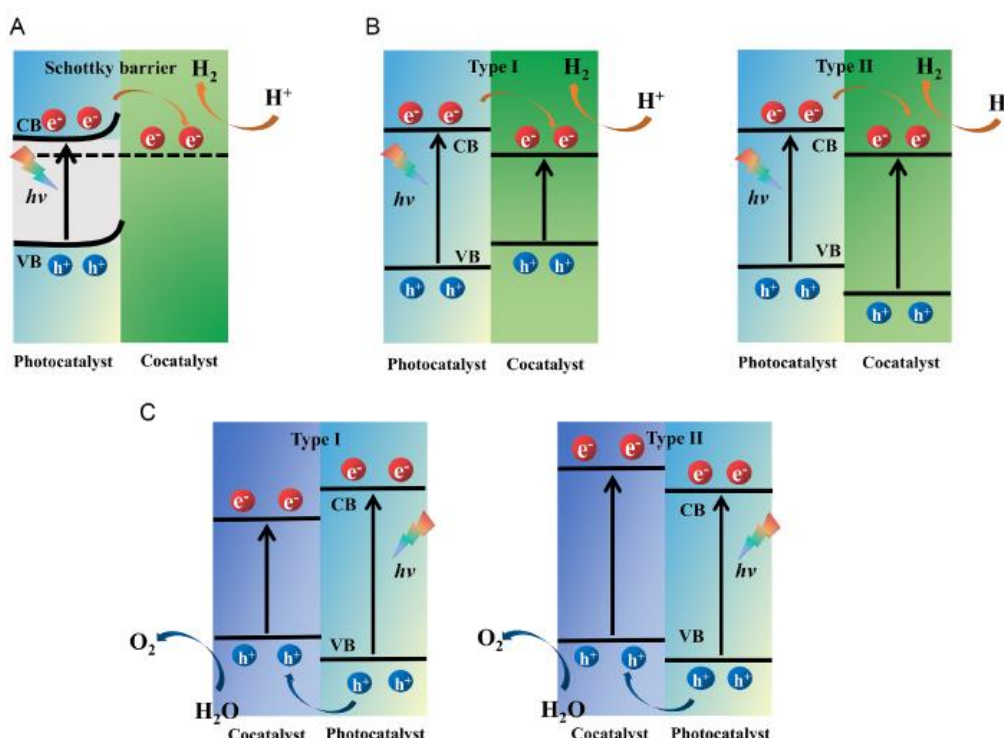


Figure 11: Schematic diagram of charge transfer through: A) Schottky barriers and B) heterojunctions for photocatalytic H_2 evolution in the semiconductor/transition metal-based co-catalyst system; C) Schematic diagram of charge transfer through heterojunctions for photocatalytic O_2 evolution in the semiconductor/transition-metal-based cocatalyst system[68]

The mechanisms regarding charge transfer fall into two categories. The first one is associated with metallic cocatalysts, including pure metals, and the second one is semiconducting cocatalysts which include metal oxides and hydroxides. Metallic cocatalysts tend to form Schottky barriers with the photocatalysts that end up forming a built-in electric field. Analytically, in the metal-semiconductor interface, an energy barrier is formed called the Schottky barrier (**Figure 11A**). In this occurrence, the bands bend at the interface so that only electrons with elevated energy can overcome this barrier. The electrons with sufficient energy, transfer to the metal through the barrier until the Fermi levels of semiconductor-metal become equal. This way both separation of carriers and transportation is achieved and metal nanoparticles act as active sites, or reductive sites for electrons, enhancing H₂ evolution.

The Semiconducting cocatalyst mechanism on the opposite, is based on the formation of appropriate band alignments with photocatalysts. In **Figure 11B** the bands alignment can look either like type I or type II, where in both cases the transfer of electrons toward the cocatalysts takes place.

The loading methods of cocatalysts have a great impact on these systems and define their overall photocatalytic efficiency. In situ loading procedures include hydrothermal or solvothermal treatment, precipitation, impregnation, electrostatic self-assembly, photodeposition and, thermal treatment and usually promote good interface contact between cocatalyst and, semiconductor. The ex-situ procedures include ultrasonic treatment, grinding and physical mixing offering better control of the size and morphology of cocatalysts and semiconductors.

1.3.1 Photodeposition of cocatalysts

When an aqueous solution of metal salt and semiconductor is illuminated, deposition of metal (oxide) nanoparticles on the semiconductor's surface takes place. Thus, photodeposition, is considered an easy way of depositing/loading metal (oxide) nanoparticles. It has been proven that loading transition-metal-based or metallic cocatalysts through photodeposition charge splitting and photocatalytic activity were favored in comparison with other techniques. This is stemming from the intimate contact of cocatalyst/semiconductor, the smaller charge transfer pathways, the nanosized and better dispersed particles and the numerous surface active sites that this technique offers. In addition, the lack of harsh conditions like temperature or pressure and its availability in room temperature under light irradiation surely add to the advantages. It has to be mentioned that there is an optimum loading as both too high and too low can harm photocatalytic efficiency. In the first case, with insufficient loading the full photocatalytic potential cannot be exploited and the excessive loading deteriorates the performance due to covering active sites, or the photocatalyst's surface area or it contributes to charge recombination.

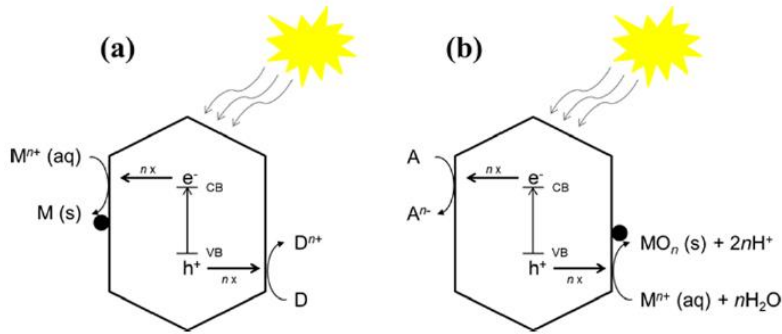
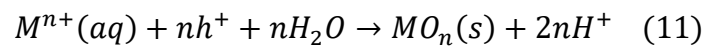
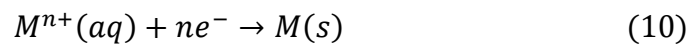


Figure 12: Schematic overview of (a) reductive photodeposition and (b) oxidative photodeposition. Where M =metal, D =(sacrificial) electron donor, A =(sacrificial) electron acceptor and n =number of electrons (or holes) involved [71]

Photodeposition that is based in light induced electrochemistry, can either be reductive (equation 10), that ends up with deposition of metallic nanoparticles, or oxidative (equation 11) that leads to the formation of metal oxide nanoparticles (Figure 12).



The photodeposition of co-catalysts is largely dependent on various factors related to illumination conditions (e.g., illumination light, light intensity, and illumination time), solution conditions (e.g., complex agent, sacrificial agent, pH of solution, precursor of cocatalyst, and amount of precursor), and semiconductor microstructures (e.g., exposed crystal facet and composition). Therefore, in the photodeposition of cocatalysts, these factors should be optimized to obtain high-efficiency cocatalysts for photocatalytic water splitting over different semiconductors. Additionally, some requirements must be met. Firstly, the oxidation/reduction potential of the metal (oxide) to be deposited must lay in between the VB and CB of the semiconductor. So, the CB must be more negative than the metal's reduction potential and the VB needs to be more positive than the oxidation potential or the species to be oxidized whether that is a metal ion, water or a sacrificial agent.

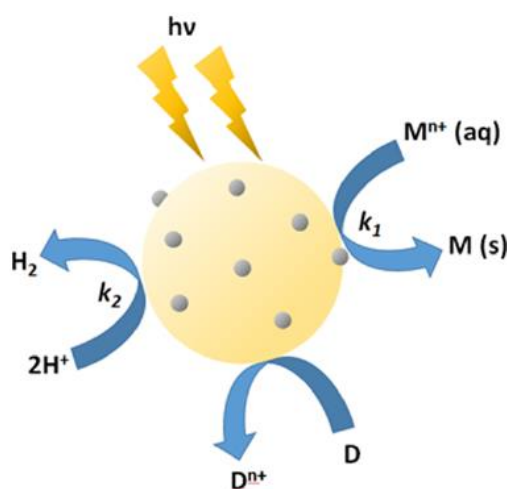


Figure 13: Scheme of reactions occurring during in situ photodeposition. A metal cation is reduced on the surface of the photocatalyst (k_1), while protons are reduced to form hydrogen (k_2). When the metal cation concentration approaches zero, the performance of a specific metal loading can be determined in the evolution of hydrogen. In this example, a sacrificial reagent D is used as hole scavenger [71]

An example can be seen in **Figure 14** where the band positions of SrTiO_3 and CaTiO_3 allow metallic Zn, Fe, Ni, Cu, Pt and Co to be deposited, whereas for metallic La, Mg and Mn this is not possible due to the more positive CB than the metal reduction potential. Secondly, the incident light must be of higher energy than the E_g of the semiconductor. Finally, charge carrier separation and migration should be possible and enough active sites on the photocatalyst's surface should be provided (**Figure 13**).

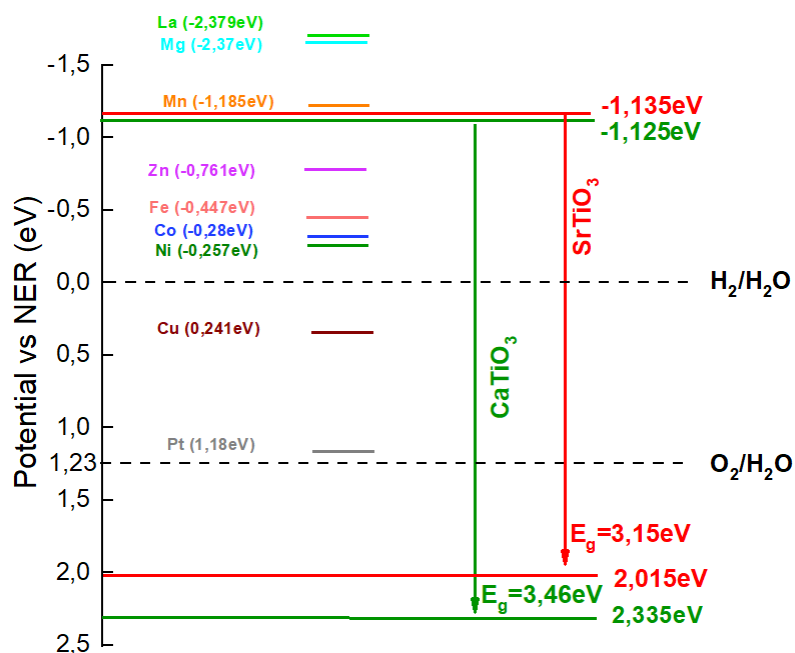


Figure 14: Schematic overview of $SrTiO_3$ and $CaTiO_3$ band positions in regard with the reduction potential of different metals

The factors that influence the outcome in this technique are, the sacrificial agent, the pH, the metal precursors, the temperature in which the procedure takes place and the presence of oxygen. The morphology, disparity and oxidation state of the nanoparticles depend heavily on these factors. However, it is not possible to predict which factor will impact what, owing to the uniqueness of each system.

In the following table (**Table 1**) a literature review can be seen regarding $SrTiO_3$ with photodeposited metals and where these composites found application. For instance, photodeposited STO was studied for overall water splitting and H_2 production as well, for photocatalytic degradation of organic pollutants, for photo-assisted dry reforming of methane and for photoreduction of CO_2 . As far as H_2 production is concerned noble metals like Pt, Pd, Au and Ag are most used as metallic cocatalysts.

Table 1: A table of papers that SrTiO₃ was used as a photocatalyst and different metals were deposited through photodeposition.

#reference	metal loading	application	H ₂ rate (μmoles/hg)
[72]	1,0wt% Pt	H ₂ evolution	24,22
[73]	0,5wt% Pt	H ₂ evolution	406,704
[74]	0,075wt% Pt	H ₂ production	8,21 10 ⁻³
[75]	0,5wt% Pt	H ₂ evolution	1200
[76]	Pt	H ₂ evolution	1766,6
	Cu		2766,6
	Au		303,3
	Ag		102,6
	Ir		15
	Pd		174,6
	Rh		119,3
[77]	5,0wt% Pd	photodegradation of bisphenol A (BPA) and 4-chlorophenol (4CP) under solar light	
[78]	Ru	Photo-assisted dry reforming of methane	
[79]	Rh + Cr	photocatalytic overall water splitting	81,8
[80]	Rh + Cr		
[81]	Ag	photoreduction of CO ₂	
[82]	Ag	photocatalytic H ₂ production	
[50]	Pt, Ru, Rh	photodegradation of organic pollutant phenol	
[83]	0,5wt% Cu	photocatalytic activity for hydrogen evolution from methanol aqueous solution	3291,6
[84]	Pt, PbO ₂	photocatalytic hydrogen and oxygen evolution	
[85]	PbCrO _x	photocatalytic Overall Water Splitting	
[86]	Ag	degradation of Methylene Orange	
[87]	Pt	photocatalytic overall water splitting	
[88]	0,5wt% Pt	Photocatalytic Hydrogen Evolution	2266
[60]	1,5wt% Pt	Photocatalytic Hydrogen Evolution	
[89]	Ag	Photocatalytic organic dye degradation	

1.4 Master Thesis objective

Sustainable and clean energy is one of the main challenges that humanity has to overcome. Beginning with the notion of drifting away from fossil fuels that harm our planet, H_2 could be the right choice since it has the potential of green fuel. Its abundance, non-toxicity and the ability to obtain it through renewable sources have made it a compelling fuel candidate. Photocatalytic water splitting for H_2 production could play an important role for the aforementioned reasons. Hence, the need for more efficient and cost effective photocatalysts has been created. Additionally, the majority of photocatalysts used for H_2 production have a wide band gap, meaning that the visible part of the electromagnetic spectrum cannot be sufficiently exploited. The scope of this master thesis is a systematic investigation of the effect of metal nanoparticles as co-catalysts on the surface of $SrTiO_3$ and $CaTiO_3$ for photocatalytic H_2 production under UV and visible light irradiation. Thus, photodeposition, that is a simple process that does not require harsh conditions, was employed to deposit metals on the surface of $SrTiO_3$. Typically, noble metals are known to enhance the photocatalytic activity and the absorbance in the visible part of the spectrum. However, noble metals increase the cost due to their scarcity. Herein, beginning from Pt as a starting metal, transition metals Ni and Cu were also studied in an effort to diverge from noble metals. Even if non-noble metals have low costs, they usually display lower hydrogen evolution rates in contrast to noble metals. Finally, photocatalytic experiments in solar and visible irradiation were carried out to confirm the photocatalytic activity and the stability of the photocatalysts was examined as well.

Chapter 2 – Experimental Section

All chemicals that were used in this thesis for the synthetic procedures and for the photocatalytic experiments were used without further purification. For the synthesis of SrTiO_3 and CaTiO_3 the metal precursors that were used were $\text{Sr}(\text{NO}_3)_2$ (99%), $\text{Ca}(\text{OH})_2$ (96%) and titanium butoxide (TBOT) (97%) and were purchased from Sigma-Aldrich. The solvent that was used was ethylene glycol $\text{HOCH}_2\text{CH}_2\text{OH}$ (EG) (99.5%) and it was purchased from Honeywell, also Sodium hydroxide pellets (NaOH) (98.0%) were purchased from Sigma-Aldrich. The precursors of the deposited metals were H_2PtCl_6 , $\text{Cu}(\text{NO}_3)_2$ and $\text{Ni}(\text{Cl}_2) \cdot 6\text{H}_2\text{O}$ from Sigma-Aldrich. The sacrificial agent used in photodeposition and photocatalytic experiments was triethanolamine (TEOA) and methanol purchased from Sigma-Aldrich

2.1 Synthesis of metal titanates

2.1.1 Synthesis of STO and CTO

For the synthesis of STO, 1,7gr of TBOT were dissolved in 25mL of EG through 15min vigorous stirring. Then 10mL (0,5M) of $\text{Sr}(\text{NO}_3)_2$ or $\text{Ca}(\text{OH})_2$ were added dropwise to the solution. Finally, 5mL (5M) of NaOH were slowly added dropwise as well. The final solution was transferred into Teflon-lined stainless steel autoclave and heated at 180°C for 24h. When the autoclave reached room temperature the precipitates were collected through centrifugation, washed with deionized water 3 times and with ethanol 1 time and dried overnight at 60°C . In the case of CTO the final powder was annealed at 600°C for 2 hours in air (heating rate $5^\circ\text{C}/\text{min}$).

2.2 Photodeposition of metals supported on metal titanates

2.2.1 Photodeposition of Pt nanoparticles on STO

The Pt-loaded STO catalysts were synthesized through a photochemical reduction method. In a typical procedure, 100mg of STO were dissolved in an aqueous solution (20 ml) containing 20% (v/v) methanol under vigorous stirring. Then, a nominal amount of H_2PtCl_6 dissolved in water (1 mg mL^{-1}) was added to the above suspension under stirring, and the resulting mixture was purged with argon for 30 min. The solution was purified under continuous stirring with Ar for 30min and was irradiated for 1h under continuous stirring with a Xe 300Watt lamp at room temperature. The Pt content in each Pt-loaded catalyst was confirmed by energy dispersive X-ray spectroscopy (EDS).

2.2.2 Photodeposition of Ni and Cu nanoparticles on STO

In a typical Photodeposition process of Ni and Cu on the STO surface, 100mg of STO were dissolved in a 20mL aqueous solution containing 12,5%(v/v) TEOA through sonication for 5min. Next, the appropriate aliquots of 1 mg mL⁻¹ Cu(NO₃)₂ aqueous solution or 1 mg mL⁻¹ NiCl₂·6H₂O aqueous solution (corresponding to the desired loadings of Cu or Ni respectively) were added to the above solution. The solution was purified under continuous stirring with Ar for 30min and was irradiated for 1h under continuous stirring with a Xe 300Watt lamp at room temperature.

2.3 Structural, morphological and optical properties

2.3.1 X-ray diffraction (XRD)

A Bruker AXS D8 Advance copper anode diffractometer (CuK α radiation), equipped with a Nickel foil monochromator operated at 40 kV and 40 mA over the 2 θ collection range of 10°-80°, was used to obtain the X-ray diffraction patterns. The scan rate was 0.05° s⁻¹.

2.3.2 Scanning electron microscopy (SEM) and energy dispersive X-ray spectroscopy (EDX)

Elemental microprobe analyses were performed by a JEOL JSM-6390LV scanning electron microscope (SEM) equipped with an Oxford INCA PentaFETx3 energy dispersive X-ray spectroscopy (EDS) detector (Oxfordshire, UK). Data acquisition was performed at least five times for each sample using an accelerating voltage of 20 kV and a 100-s accumulation time.

2.3.3 Transmission electron microscopy (TEM)

The microscopic nanostructures were studied by transmission electron microscopy (TEM) operating at 200kV (JEM-2100 instrument equipped with LaB₆ filament). Samples were prepared by suspending fine powders in anhydrous ethanol and then drop casting on a copper grid covered with carbon film.

2.3.4 Ultraviolet–visible spectroscopy (UV-Vis)

The UV – Visible diffuse reflection spectra of the powders were measured on a Perkin-Elmer Lambda 950 UV-VIS-NIR spectrophotometer, using BaSO₄ powder, as a

reference reflectance spectrum. The measured diffuse reflectance was converted to absorption using the Kubelka- Munk function (F(R)) (**equation 12**)

$$K.M.function = F(R) = \frac{k}{S} = \frac{(1 - R)^2}{(2R)} \quad (12)$$

$$[F(R) \cdot hv]^{\frac{1}{2}} = A (E_g - hv) \quad (13)$$

R is the measured Reflectance, k and S are the absorption and scattering coefficients. For the estimated E_g of the materials **equation 13** was used, hv is the photon energy and $n=2$ for indirect and $n=1/2$ for direct bandgap. In this case **equation 13** with $n=2$ was used. Hence, the E_g was found by plotting $[F(R) \cdot hv]^{1/2}$ vs photon energy, hv (eV).

2.3.5 Impedance spectroscopy

Electrochemical impedance-potential measurements were performed using a single-channel potentiostat/galvanostat Princeton Applied Research VersaSTAT 4 equipped with a three-electrode cell, consisting of a sample-coated Fluorine-doped tin oxide (FTO, $10\Omega/\square$) glass ($1.0 \times 2.5 \text{ cm}^2$) as working electrode, an Ag/AgCl (saturated KCl) reference electrode, and a Pt-mesh counter electrode. To fabricate the working electrodes, a catalyst ink was made by dispersing 10 mg of each sample in 1 mL Ethanol. Then, 40 μL Nafion solution (5 wt.%) was added and the mixture was ultrasonicated for 30 min and left under stirring for 24 h. When a uniform suspension was formed, 50 μL of the solution was drop-casted on the conductive surface of a clean FTO glass electrode (effective surface 1 cm^2) and the film was dried at 40–50 $^\circ\text{C}$ for 1h and then heated at 150 $^\circ\text{C}$ for 1h before electrochemical tests.

For the Mott-Schottky (M-S) plots, the space-charge capacitance (C_{sc}) of the electrode/electrolyte interface was measured in 0.5 M Na_2SO_4 (pH=7) electrolyte, at 1 kHz frequency, using a 10 mV AC voltage amplitude, and the measured potentials were converted to the reversible hydrogen electrode (RHE, pH=7) scale using the formula $E_{\text{RHE}} = E_{\text{Ag/AgCl}} + 0.194$, where E_{RHE} is the potential in the RHE scale and $E_{\text{Ag/AgCl}}$ is the measured potential in the Ag/AgCl scale.

The donor density (N_D) of the as-prepared materials was estimated from the slope of the linear portion of the Mott-Schottky plots, according to the Mott–Schottky (M-S) equation:

$$N_D = \frac{2(E - E_{FB}) \cdot C_{SC}^2}{\epsilon \epsilon_o e_o} \quad (14)$$

where N_D is the donor density of electrode material, E is the applied potential, E_{FB} is the flat band potential, C_{SC} is the space charge capacitance, ϵ_o is the dielectric permittivity, e_o is the elementary charge and ϵ is the relative dielectric constant of the tested material; ($\epsilon_o = 8.8542 \times 10^{-12}$ F/m = 8.8542×10^{-10} F/cm, $e_o = 1.602 \times 10^{-19}$ C and $\epsilon = 340$ for STO according to literature reports[90][91]).

In the M-S equation, the term $(E - E_{FB}) \cdot C_{sc}^2$ is the reciprocal of the slope (k) of the Mott-Schottky plot, thus it can be simplified to:

$$N_D = \frac{4.147 \times 10^{25}}{k} \cdot \frac{cm}{F \cdot C} \quad (15)$$

2.3.6 Photoluminescence (PL)

For the room temperature PL measurements, an excitation wavelength of 320 nm was used and the emission spectrum was recorded at a wavelength range of 360-450 nm.

2.3.7 Photocatalytic experiments for H₂ evolution

The photocatalytic reduction of water towards H₂ evolution reaction (HER) was performed in a water-cooled Pyrex reaction vessel, which was irradiated with a 300 W Xenon lamp, equipped with cut-off filters (360 nm and 420 nm cut-off, respectively). All the experiments were carried out at 20 ± 2 °C using a water bath cooling system. In the pyrex reactor the catalyst was suspended with vigorous stirring in 20% (v/v) aqueous triethanolamine solution (20 ml). The suspension was first purged with Ar flow for at least 30 min to ensure complete removal of oxygen and then irradiated. The produced H₂ gas was detected by taking 100 µL of gas using a gas tight syringe and was analyzed by GC (Shimadzu GC-2014 equipped with a TCD detector), using Ar as the carrier gas.

Chapter 3 Results and discussion

3.1 Characterization of metal titanates

3.1.1 Structural characterization

In **Figure 15** the XRD pattern of STO can be seen in association with the reference patterns of STO and TiO_2 . The sample is not pure phased, as peaks belonging to TiO_2 can be detected. Moreover, the STO peaks at $22,7^\circ$, $32,3^\circ$, $39,9^\circ$, $46,4^\circ$, $52,3^\circ$, $57,7^\circ$, $67,8^\circ$, $72,5^\circ$ and at $77,1^\circ$ that correspond to (100), (110), (111), (200), (210), (211), (220), (221) and (310) planes belong to cubic system. The peaks at $25,25^\circ$, $25,81^\circ$ and $36,20^\circ$ corresponding to planes (210), (111) and (102) are assigned to TiO_2 orthorhombic crystal system.

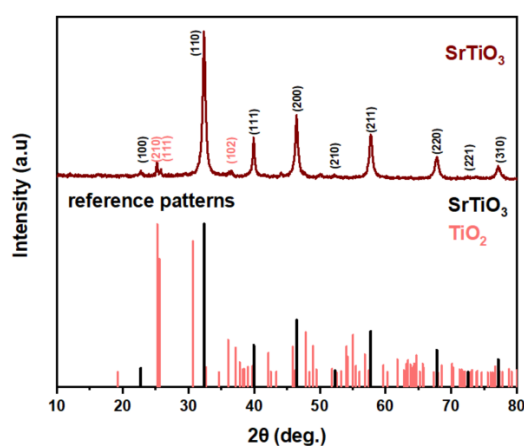


Figure 15: XRD pattern of STO and reference patterns of STO and TiO_2

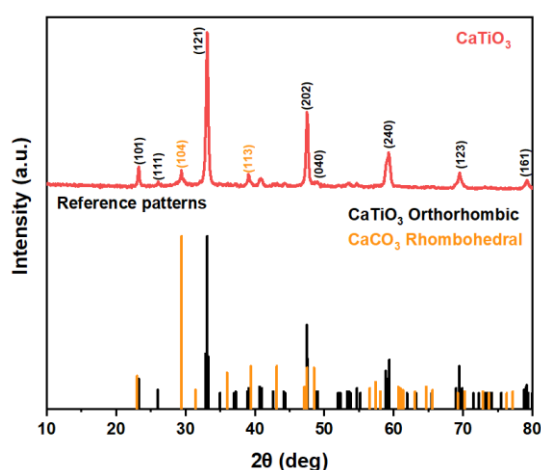


Figure 16: XRD pattern of CTO and reference patterns of CTO and CaCO_3

As for the XRD pattern of CTO it can be seen from **Figure 16** that it is not pure phased either as there are 2 peaks assigned to CaCO_3 . The peaks at 23° , 26° , 33° , 47° , 39° , 59° , 69° and 79° corresponding to planes (101), (111), (121), (202), (040), (240), (123) and (161) are assigned to cubic CaTiO_3 and the peaks at 29° and $39,9^\circ$ corresponding to planes (104) and (113) are assigned to rhombohedral CaCO_3 .

3.1.2. Morphological characterization

From the SEM and TEM images (**Figure 17**) the morphology of STO can be seen. The sample is made up from small nanoparticles of irregular round shapes that are ~20nm-30nm is size, bigger nanoparticles comprised by smaller ones can also be spotted, also in round shaped, that are approximately 150-200nm in size. EDX data seen in **Figure 18** confirm the existence of Sr and Ti atoms and that their stoichiometry is 1:1 as well

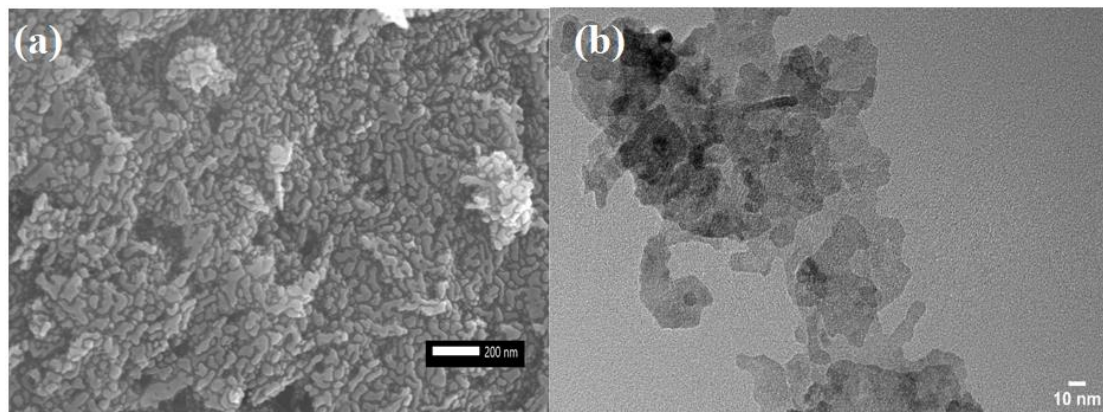


Figure 17: SEM image of STO (a), TEM image of STO (b)

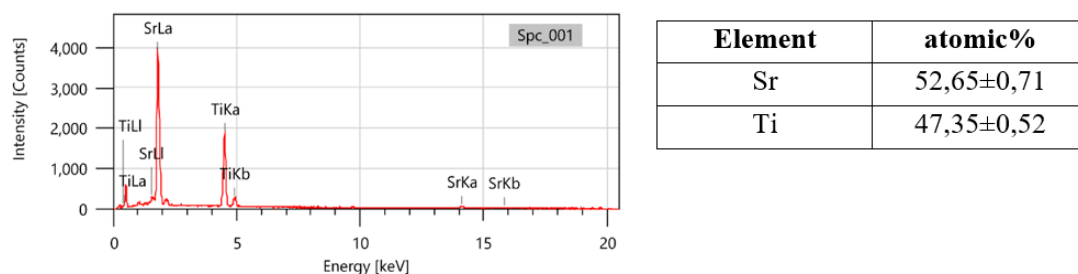


Figure 18: EDX data of STO

3.1.3. Optical characterization

Diffuse reflectance spectrum was used to analyze the photo-responsive characteristics of STO. As illustrated in **Figure 19 (a)** STO exhibits a strong absorption in the ultraviolet region with wavelengths smaller than 400nm. From the corresponding Tauch plot (**Figure 19 (b)**) the bandgap was estimated 3,11eV, using the Kubelka-Munk formula for indirect bandgap semiconductor, agreeing with literature that it is a wide bandgap semiconductor activated with UV irradiation[15].

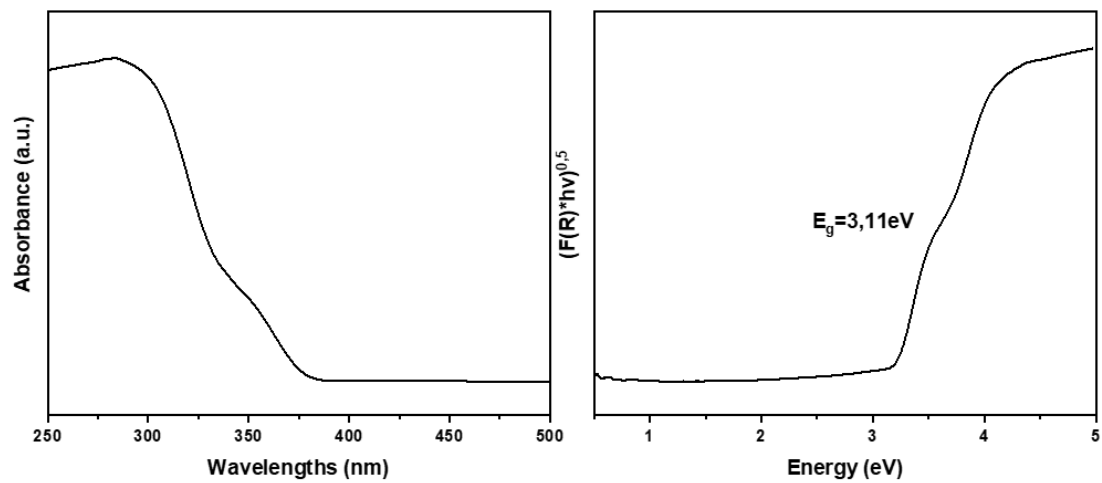


Figure 19: (a) UV-vis diffuse reflectance spectrum and (b) Tauch plot from which the E_g was extracted with axis $((F(R) \cdot hv)^{1/2} - hv)$, where $F(R)$ is the absorbance coefficient, $h\nu$ is the photon energy (h is the Planck constant and ν is the light frequency) and $1/2$ was chosen because STO is a semiconductor with indirect bandgap.

3.2 Active catalysts (Pt, Cu, Ni) supported on STO

Firstly, STO was synthesized and characterized and based on that three series of samples were synthesized through photodeposition with the three metals (Pt, Ni and Cu). On the next table (**Table 2**) an overview of the samples and the metal loadings (wt%) can be seen.

Table 2: the synthesized samples and their metal loading (wt%)

Metal loading (wt%)
Pt 0,1%
Pt 0,2%
Pt 0,37%
Pt 0,4%
Pt 0,56%
Ni 0,1%
Ni 0,25%
Ni 0,5%
Ni 3,6%
Cu 0,1%
Cu 0,5%
Cu 1%
Cu 5%

3.2.1 Pt catalysts supported on STO

3.2.1.1. Structural properties

The XRD patterns of STO and STO Pt decorated samples is illustrated in **Figure 20**. Due to the small amount of loading and the small grain size of Pt nanoparticles there is no difference in the patterns, as no peaks assigned to Pt can be spotted. In **Table 3** the EDX data regarding the percentage of Pt in the samples can be seen. It is confirmed that the theoretical and experimental percentage are similar with small deviations. It has to be mentioned that EDX data from the samples with Pt loading 0,09%-0,2% could not be obtained since the percentage is too small to be detected.

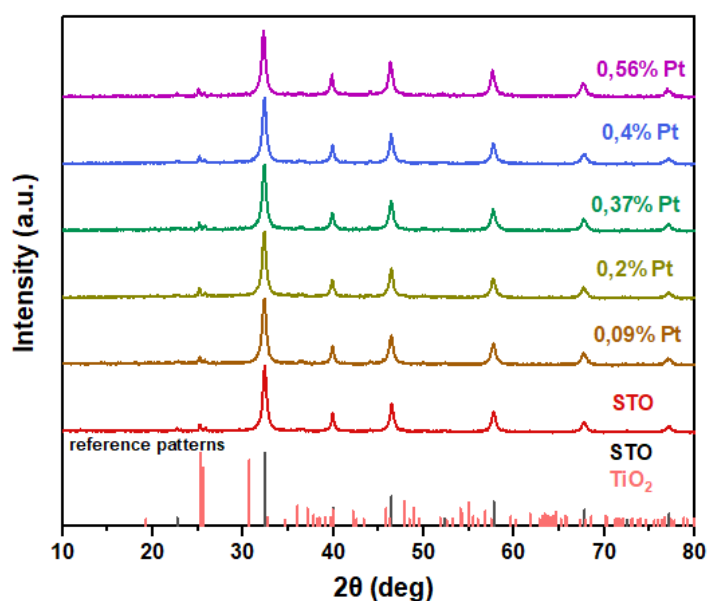


Figure 20: XRD pattern of STO and Pt decorated STO, as well as reference patterns of STO and TiO

Table 3: EDS data of STO-Pt samples

Theoretical % of Pt	Experimental % of Pt
0,09%	-
0,2%	-
0,37%	-
0,4%	0,4%
0,56%	0,5%

3.2.1.2 Morphological properties

In agreement with the EDX data the existence of Pt nanoparticles is confirmed by HRTEM images seen in **Figure 21 (c)** where two type of lattice fringes can be spotted, 0,27nm and 0,22nm corresponding to planes (110) of STO and (111) of metallic Pt respectively. The Pt nanoparticles seem to be well and uniformly dispersed on the STO with no significant aggregation (**Figure 21 (a,b)**). The particle size distribution was estimated by measuring dimensions of nanoparticles from HRTEM images and the average value calculated was based on measurements of 61 particles. So, the as-deposited nanoparticles exhibit very narrow size distribution, with sizes ranging from 1,5 to 3,5 nm with the average value calculated at $d=2,44 \pm 0,36\text{nm}$ (**Figure 22**), which is a value close to what is expected from the literature [92].

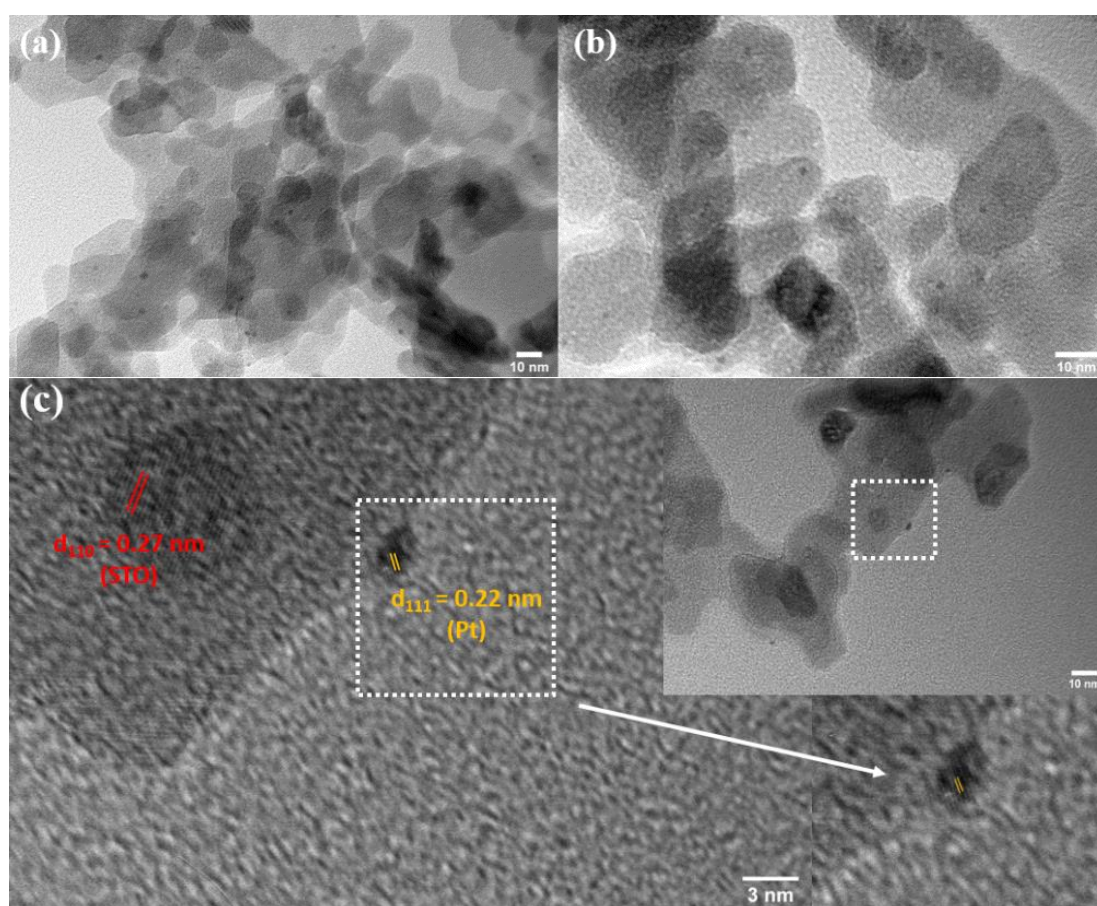


Figure 21: TEM images of STO-Pt 0,4wt%

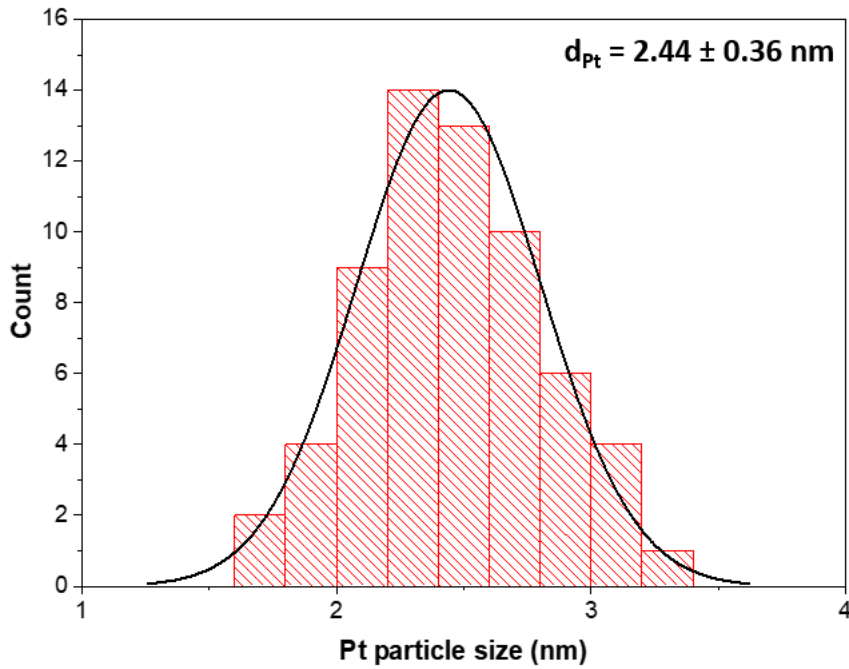


Figure 22: particle size distribution of photodeposited Pt nanoparticles on STO

3.2.1.3 Optical properties

The optical properties of the STO-Pt samples were investigated through Diffuse reflectance spectrum. In **Figure 23** the absorbance spectra and Tauch plots can be seen. In the samples where Pt was deposited there is a slight shift in the absorbance towards the visible wavelengths, again agreeing with the EDX and HRTEM data that the metal indeed exists on the STO surface. The bandgaps were calculated and the values of E_g slightly decrease from 3.11 eV to 2.96 eV. Additionally, an increase in the absorbance at wavelengths higher than 400 nm is seen that could imply that the samples may be activated through visible irradiation. It has to be mentioned that with photodeposition the bandgap of STO does not change as it is an intrinsic property. The minor shifts that are observed are associated with the absorption properties of the nanoparticles deposited that are superimposed on the original spectrum.

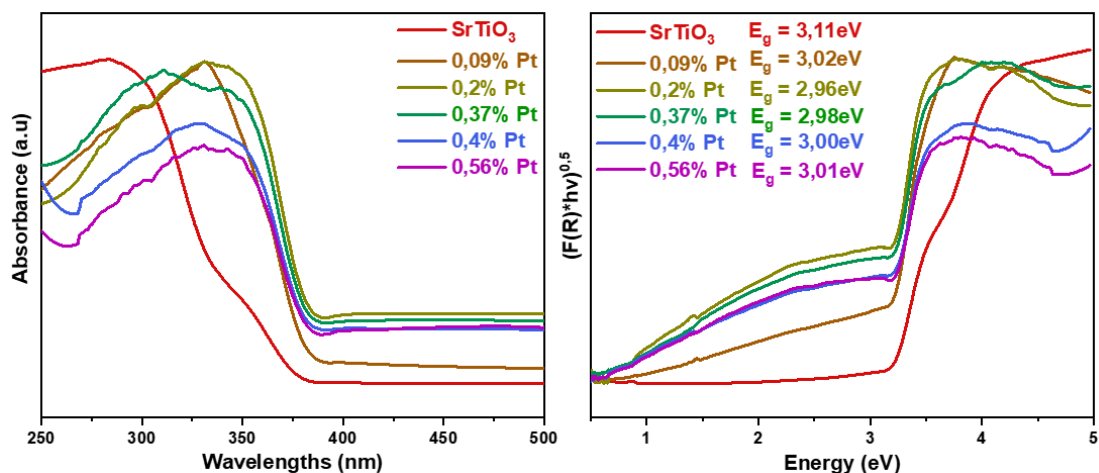


Figure 23: a) UV-vis diffuse reflectance spectrum of STO-Pt samples and (b) Tauc plot from which the E_g was extracted with axis $((F(R) \cdot hv)^{1/2} - hv)$, where $F(R)$ is the absorbance coefficient, $h\nu$ is the photon energy (h is the Planck constant and ν is the light frequency) and $1/2$ was chosen because STO is a semiconductor with indirect bandgap

Figure 24 displays the photoluminescence (PL) emission spectra recorded for the STO, 0.1wt%Pt-STO, 0.4wt% Pt-STO and 0.56wt% Pt-STO catalysts under excitation with 320 nm light. PL measurements reveal the transport and recombination dynamics of the photogenerated carriers. The intense PL emission at 379 (3.18eV) corresponds to the photon-assisted CB-to-VB optical transitions. The broad visible emission at 379nm and 404nm are probably attributed to the presence of defects [60]. Importantly, compared to pristine STO, Pt decorated STO especially the loading of 0.4wt% Pt, that has the highest photocatalytic activity as seen at the corresponding chapter, show a drastic decrease of the photoemission signal, indicating that recombination of photogenerated electrons and holes has been efficiently repressed. These results suggest that the composite material has the potential of efficient charge transport between adjusted nanoparticles, facilitating the electron-hole dissociation.

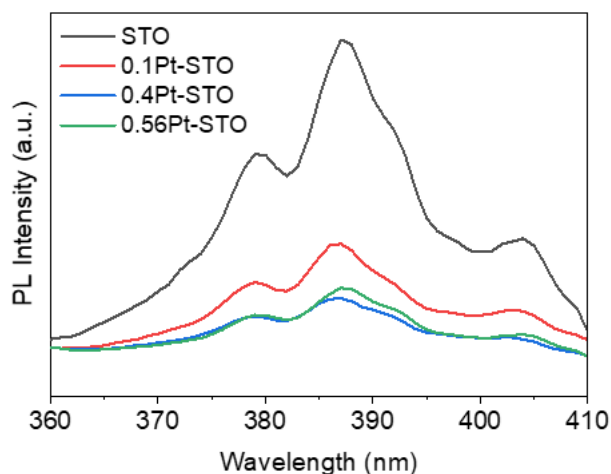


Figure 24: Room temperature PL spectra of 0,1wt%Pt-STO, 0,4wt% Pt-STO and 0,56wt% Pt-STO catalysts

3.2.2 Ni catalysts supported on STO

3.2.2.1 Structural properties

The XRD patterns of STO and STO Ni decorated samples are pictured in **Figure 25**. Again the small amount of loading is the reason that there is no difference in the patterns, as no peaks assigned to metallic Ni, oxide or even hydroxide can be seen. In **Table 4** the EDX data where the percentage of Ni in the samples can be seen. It is confirmed that the theoretical and experimental percentage are similar with small deviations for 0,25% and 0,5% loading. On the contrary, for higher percentage loadings like 3,6% the EDX percentage has high deviation from the expected percentage. The 0,1% Ni loading could not be measured in EDX in virtue of the very small loading.

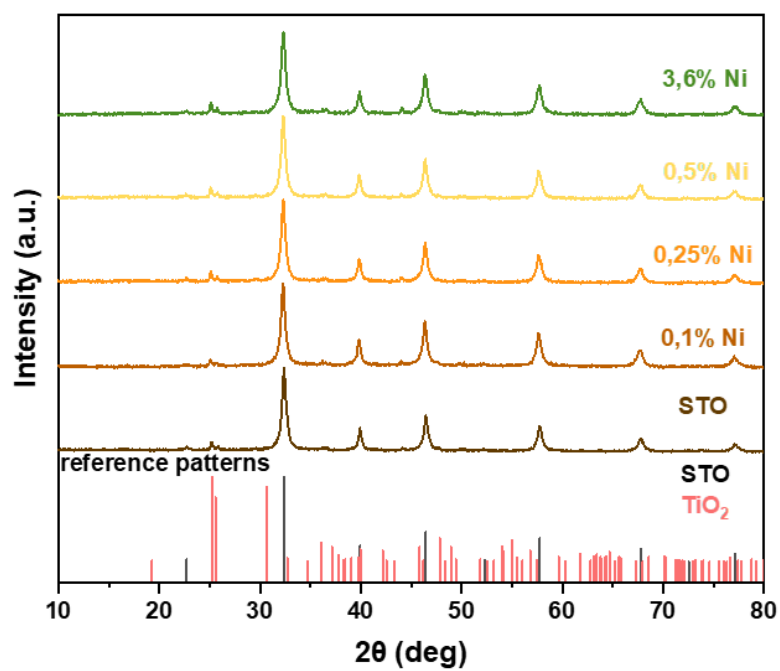


Figure 25: XRD pattern of STO and Ni decorated STO, as well as reference patterns of STO and TiO_2

Table 4: EDX data of STO-Ni samples

Theoretical %	Experimental %
0,1%	-
0,25%	0,23%
0,5%	0,44%
3,6%	1,41%

3.2.2.2 Optical properties

The optical properties of the STO-Ni samples were investigated through Diffuse reflectance spectrum. In **Figure 26** the absorbance spectra and Tauch plots can be seen. The deposition of Ni causes a slight shift in the absorbance towards higher wavelengths, and in accordance with the EDX data the existence of Ni on the STO surface is verified. The bandgaps were calculated and the values of E_g slightly decrease as the Ni loading increases with values ranging from 3,11eV to 3,02eV.

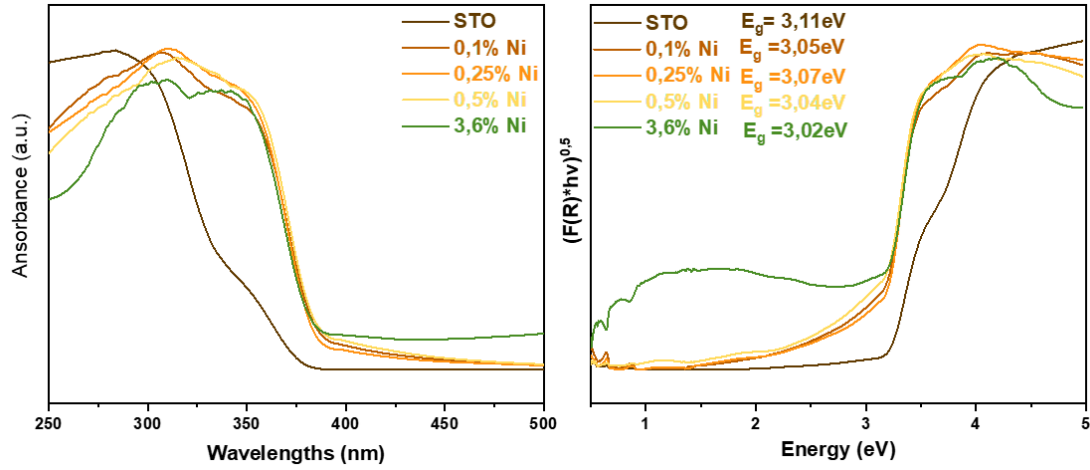


Figure 26: a) UV-vis diffuse reflectance spectrum of STO-Ni samples and (b) Tauc plot from which the E_g was extracted with axis $((F(R) \cdot hv)^{1/2} - hv)$, where $F(R)$ is the absorbance coefficient, $h\nu$ is the photon energy (h is the Planck constant and ν is the light frequency) and $1/2$ was chosen because STO is a semiconductor with indirect bandgap

3.3.3 Cu catalyst supported on STO

3.3.3.1 Structural properties

The XRD patterns of STO and STO Cu decorated samples is illustrated in **Figure 27**. Due to the small amount of loading there is no difference in the patterns, as no peaks assigned to Cu can be seen. In **Table 5** the EDX data regarding the percentage of Cu in the sampled is showed. It is confirmed that the theoretical and experimental percentage are in good agreement.

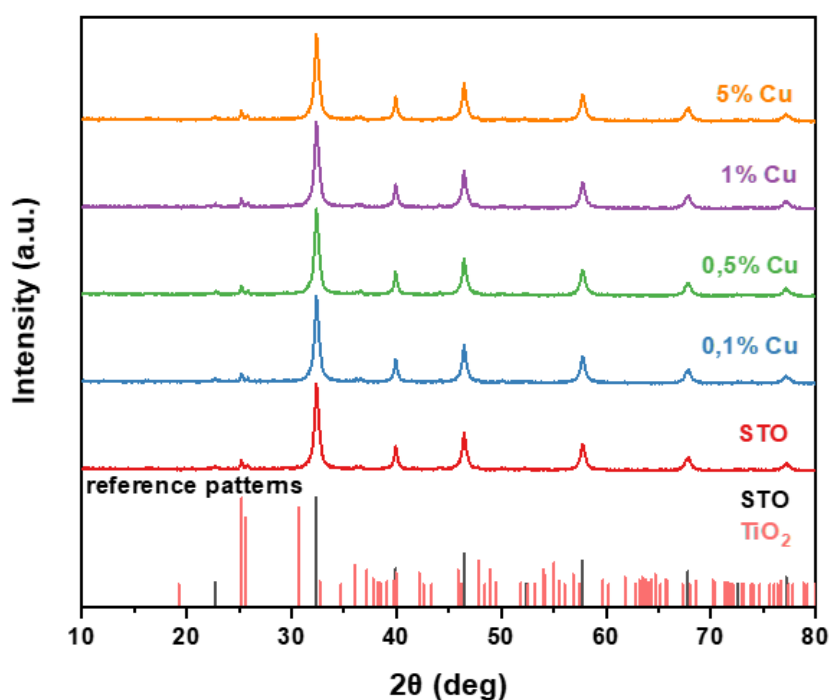


Figure 27: XRD pattern of STO and Cu decorated STO, as well as reference patterns of STO and TiO₂

Table 5: EDX data of STO-Cu samples

Theoretical %	Experimental %
0,1%	0,11%
0,5%	0,47%
1%	0,98%
5%	6,70%

3.3.3.2 Optical properties

The optical properties of the STO-Cu samples were investigated through Diffuse reflectance spectrum. In **Figure 28** the absorbance spectra and Tauch plots can be seen. The deposition of Cu as the other metals causes a slight shift in the absorbance towards higher wavelengths too. The bandgaps were calculated and the values of E_g slightly decrease as the Cu loading increases with values ranging from 3,11eV to 3,08eV.

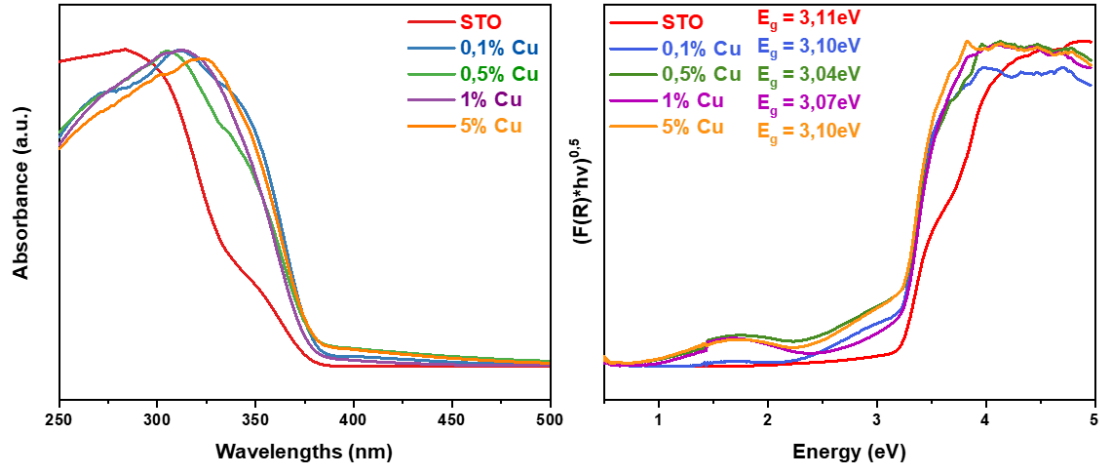


Figure 28: a) UV-vis diffuse reflectance spectrum of STO-Cu samples and (b) Tauch plot from which the E_g was extracted with axis $((F(R) \cdot hv)^{1/2} - hv)$, where $F(R)$ is the absorbance coefficient, $h\nu$ is the photon energy (h is the Planck constant and ν is the light frequency) and $1/2$ was chosen because STO is a semiconductor with indirect bandgap

3.5 Photocatalytic results

3.5.1 Hydrogen evolution of metal catalysts supported on STO

3.5.1.1 Hydrogen evolution of Pt supported on STO

In order to assess the photoactivity of the synthesized samples pristine STO and the Pt-decorated samples were evaluated by measuring the solar (UV/Vis) irradiated reduction of water towards hydrogen production. The photocatalytic experiments took place in an air tied Pyrex reactor with triethanolamine (TEOA) as the sacrificial agent. The results are compared in **Figure 29** below. As expected all Pt loadings had much higher H_2 production than pristine STO as Pt nanoparticles act like electron sinks by trapping them, thus contributing positively in charge transportation and dissociation. However, the sample with the optimum loading is the one with 0,4% Pt that exhibited a H_2 production of 632,2 μ moles in 2 hours, 8 times higher than the pristine STO. The optimum Pt loading of 0,4wt% was tested in visible light irradiation in association with unmodified STO (**Figure 30**). Although the pristine STO did not have any production as it is a wide bandgap semiconductor activated only with UV irradiation, the modified sample reached a H_2 production of just 8,7 μ moles in 2 hours of irradiation.

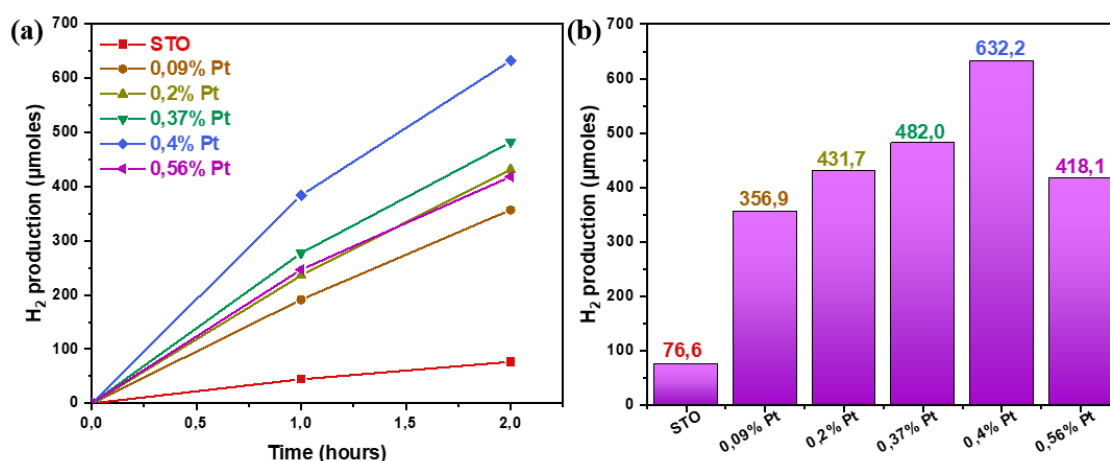


Figure 29: Photocatalytic H_2 production of STO and of Pt-decorated STO materials with different %wt of metal loadings. Reaction conditions: 20mg of catalyst, 20mL aqueous solution, 20% v/v of sacrificial agent (TEOA), light irradiation of $\lambda > 360\text{nm}$

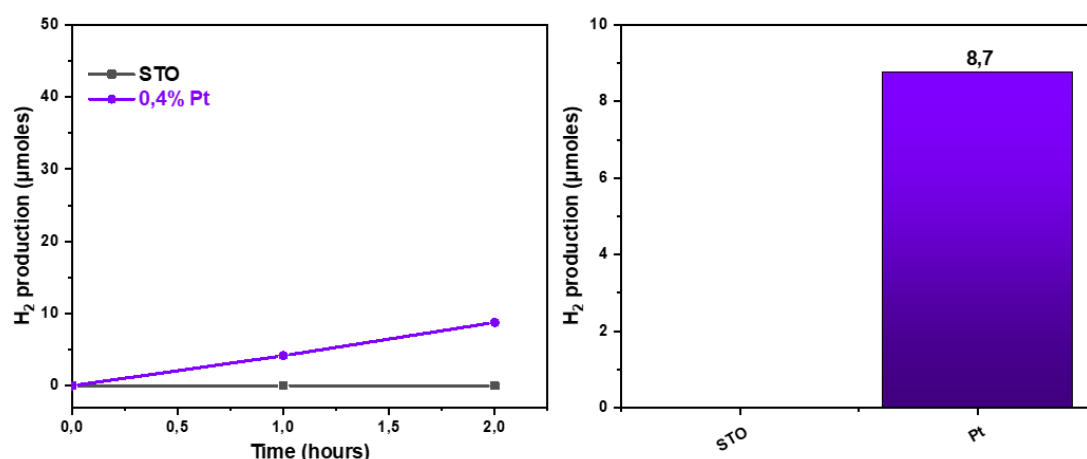


Figure 30: Photocatalytic H₂ production of STO and of Pt-decorated STO with 0.4wt% loading. Reaction conditions: 20mg of catalyst, 20mL aqueous solution, 20% v/v of sacrificial agent (TEOA), visible light irradiation

3.5.1.1.1 Photocatalytic Mechanism towards H₂ production of Pt supported on STO

To explain the observed variation in the photocatalytic activity towards H₂ production (**Figure 29**), the position of the conduction band and valence band edges of each catalyst were estimated based on electrochemical impedance spectroscopy (EIS) and optical absorption measurements. Mott-Schottky plots obtained at a frequency of 1 kHz and the corresponding fits of the linear regime of the inverse square capacitance ($1/C_{sc}^2$) versus applied potential (E) curves of STO and Pt-STO samples with various loadings of Pt (i.e. 0.1, 0.4 and 0.56 wt.%) are displayed in **Figure 31**. Using extrapolation to $1/C_{sc}^2 = 0$, the flat-band potentials of STO, 0.1wt% Pt-STO, 0.4wt% Pt-STO and 0.56wt% Pt-STO can be estimated to be -0.76, -0.57, -0.52 V and -0.55 V vs. RHE at pH=7, respectively. For all the samples, the positive slopes of the linear region of the M-S plots indicate that are n-type properties. A general trend can be identified from these results (**Figure 32**): the increase of Pt content in STO may lead to the positive shift (anodic shift) of flat-band potential due the high work function (low Fermi level) of Pt (5.65 eV)[93], which results in the formation of a Schottky junction at the Pt/STO interface. When such contact occurs, electrons can lower their energy by flowing from the semiconductor CB into the metal until the Fermi lever of STO reaches equilibrium with the chemical potential of Pt, thus resulting in a positive shift of E_{FB} of STO upon the deposition of Pt nanoparticles. However, it should be noted that the E_{FB} of the sample with higher Pt content (0.56wt% Pt-STO) is slightly negatively shifted (cathodic shift), compared to that of 0.4wt% Pt-STO, probably due to the formation of larger Pt nanoparticles on the surface of STO and the relatively poorer electron transport from

STO to the larger Pt particles[94][95]. This is also supported by the donor density measurements of the examined catalysts, where the N_D value of STO decreases substantially with increasing the Pt loading amount (due to the electron flow from STO to the Pt nanoparticles) and reaches a minimum at a Pt content of 0.4 wt/%. Further increasing the Pt loading amount to 0.56 wt%, a relatively increased N_D value for the 0.56wt% Pt-STO sample is observed, which also suggests less efficient interface contact and electron transfer between STO and Pt in this sample, presumably because of the formation of larger Pt nanoparticles. All the estimated E_{FB} and N_D values from the Mott-Schottky analysis of the examined catalysts are summarized in the following **Table 4**. The VB maximum was determined by subtracting the energy band gap (E_g) from the E_{FB} value of the semiconductors.

Table 4: Electrochemical data (pH=7) of Pt decorated STO

Sample	Flat Band E_{FB} (V vs. RHE, pH=7)	Slope k ($F^{-2}cm^4/V$)	Donor density N_D ($1/cm^3$)
STO	-0.76	0.83×10^{10}	5.022×10^{15}
0.1wt%Pt-STO	-0.57	2.41×10^{10}	1.723×10^{15}
0.4wt%Pt-STO	-0.52	9.16×10^{10}	4.525×10^{14}
0.56wt%Pt-STO	-0.55	4.24×10^{10}	9.781×10^{14}

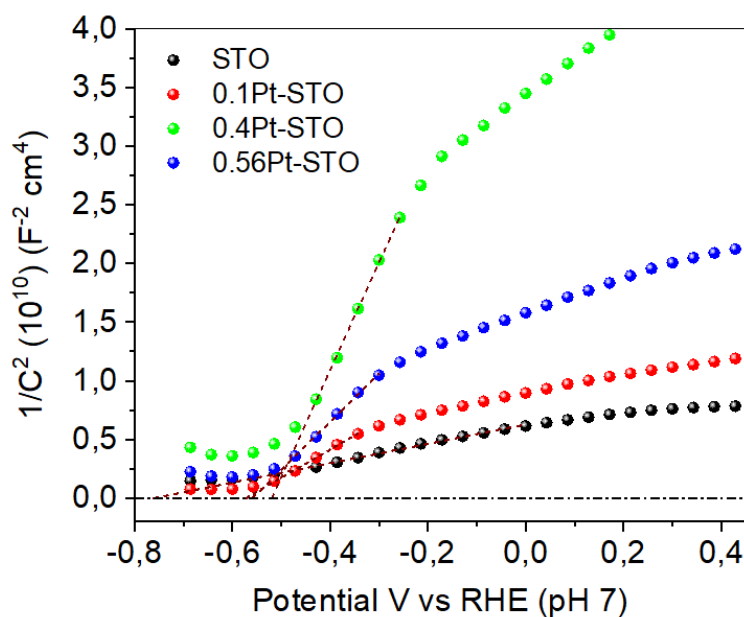


Figure 31: Mott-Schottky plots of STO and Pt-STO samples with various loadings of Pt (i.e, 0.1, 0.4 and 0.56 wt.%)

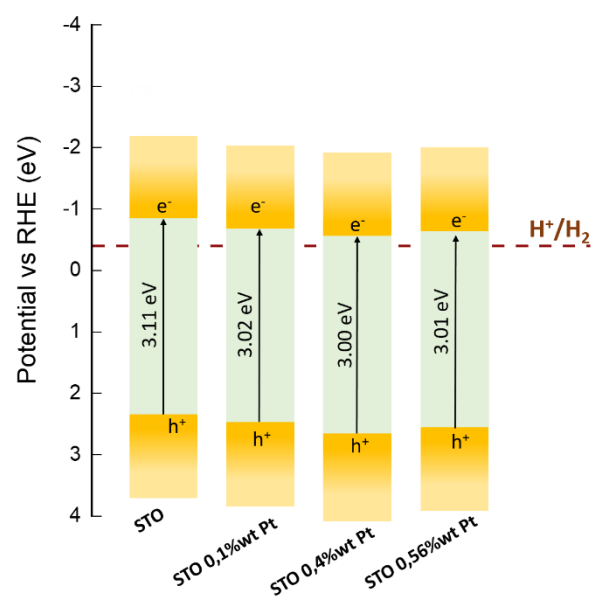


Figure 32: energy band structure of STO and Pt decorated STO samples

3.5.1.2 Hydrogen evolution of Ni supported on STO

In **Figure 33** the time course of photocatalytic H_2 evolution over STO and Ni-modified STO is illustrated. Different loadings of Ni were tested from 0,1wt% up to 3,6wt% and the optimum was proven to be 0,25wt%. Analytically, STO with 0,25wt% Ni reached a production of 171,6 μ moles at 2 hours of irradiation, that is 2,3 times higher than pristine STO. Although the increase in Ni percentage up to 0,25wt% enhances the photocatalytic activity beyond that it has the opposite effect, as 0,5wt% and 3,6wt% approach the pristine STO production. The lower photocatalytic activity beyond the optimum percentage may be due to the fact that Ni species on the STO surface act as recombination centers[96]. The sample with the optimum Ni percentage was tested in photocatalytic H_2 production in visible light irradiation (**Figure 34**). The production after 2 hours of irradiation was slightly above zero at 1,1 μ moles.

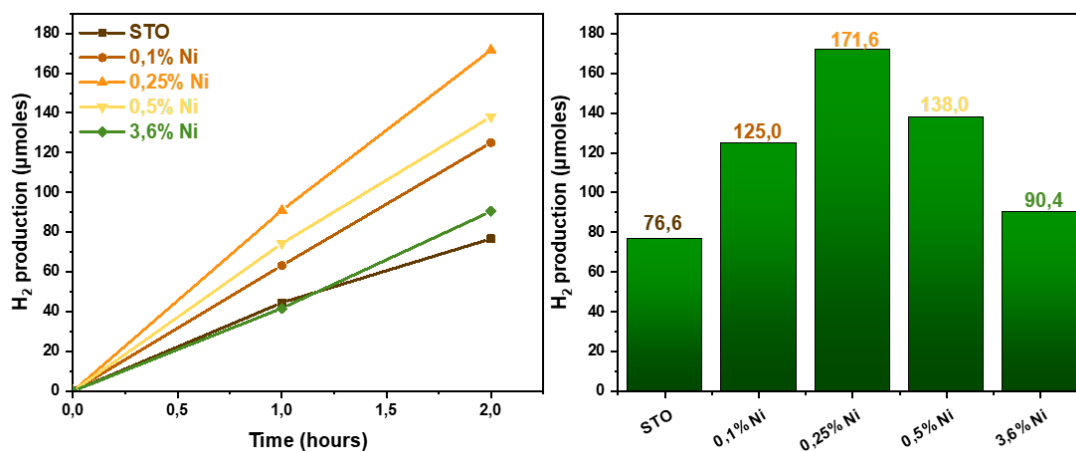


Figure 33: Photocatalytic H_2 production of STO and of Ni-decorated STO materials with different %wt of metal loadings. Reaction conditions: 20mg of catalyst, 20mL aqueous solution, 20% v/v of sacrificial agent (TEOA), light irradiation of $\lambda > 360\text{nm}$

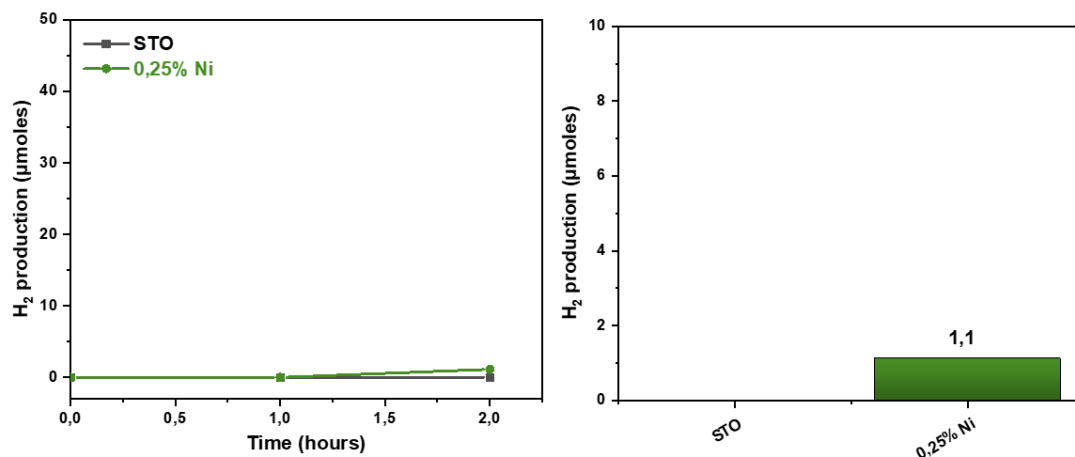


Figure 34: Photocatalytic H₂ production of STO and of Ni-decorated STO with 0,25wt% loading. Reaction conditions: 20mg of catalyst, 20mL aqueous solution, 20% v/v of sacrificial agent (TEOA), visible light irradiation

3.5.1.3. Hydrogen evolution of Cu supported on STO

In **Figure 35** the H₂ production of the samples decorated with Cu is illustrated in accordance with the pristine material. Samples were prepared with percentages of Cu varying for 0,1wt% up to 5wt%. Again as the Cu percentage augments so does the photocatalytic activity with the optimum percentage being 1wt% with a production of 138,8μmoles at 2 hours of irradiation with solar light, that is 2 times higher than STO. Further increase at the Cu percentage results in deterioration of H₂ production in virtue of Cu particles on the semiconductor's surface acting as charge recombination centers halting the whole photocatalytic reaction towards H₂ production[83]. Additionally, experiments with visible irradiation took place with the optimum percentage of 1wt% Cu (**Figure 36**). These experiments revealed that the Cu cocatalyst did not enhance the H₂ production when visible irradiation was used.

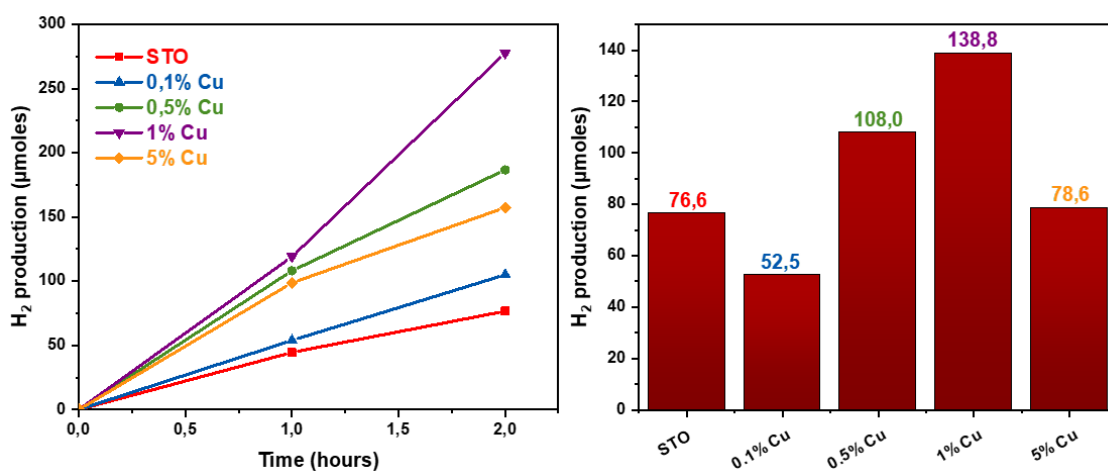


Figure 35: Photocatalytic H₂ production of STO and of Cu-decorated STO materials with different %wt of metal loadings. Reaction conditions: 20mg of catalyst, 20mL aqueous solution, 20% v/v of sacrificial agent (TEOA), light irradiation of $\lambda > 360\text{nm}$

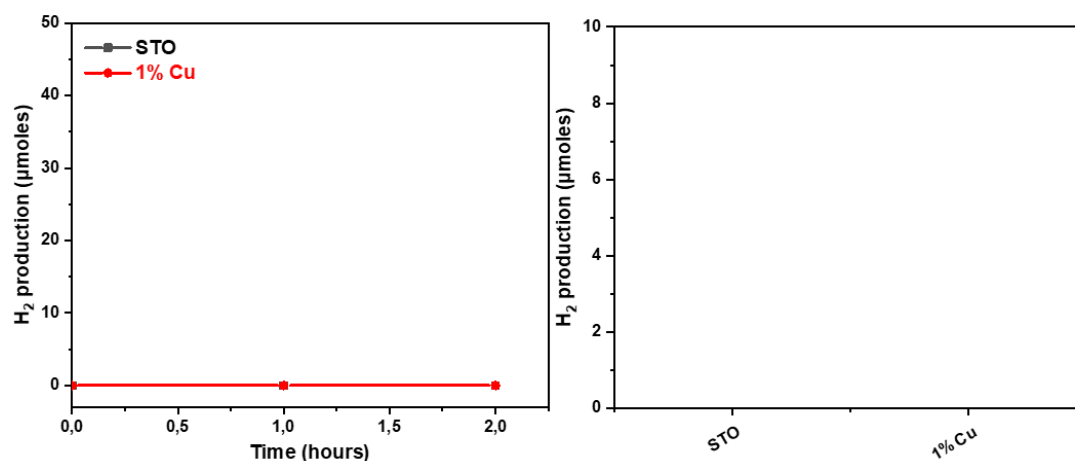


Figure 36: Photocatalytic H₂ production of STO and of Cu-decorated STO with 1wt% loading. Reaction conditions: 20mg of catalyst, 20mL aqueous solution, 20% v/v of sacrificial agent (TEOA), visible light irradiation

3.5.2. Stability

The stability of the samples with the optimum metal loadings was examined. As seen in **Figure 37** although the sample with 0,4wt% Pt exhibited a lowered H_2 production after the second run, it reached a plateau and all the other runs up until the fourth had almost the same production. Moreover, the second run corresponds to the 60% of the first run meaning that there was a 40% decrease of H_2 production, possibly due to the disassociation of some percentage of the Pt cocatalyst. Also, EDX and XRD were used to assess the stability of the catalyst after its fourth use. XRD patterns before and after are the same showing no significant alteration of the crystal structure of the catalyst. EDX data after the catalysis did not show Pt percentage probably because such small amount could not be detect. However, it was expected to be smaller than 0,4wt% as the photocatalytic activity decreases after the first cycle.

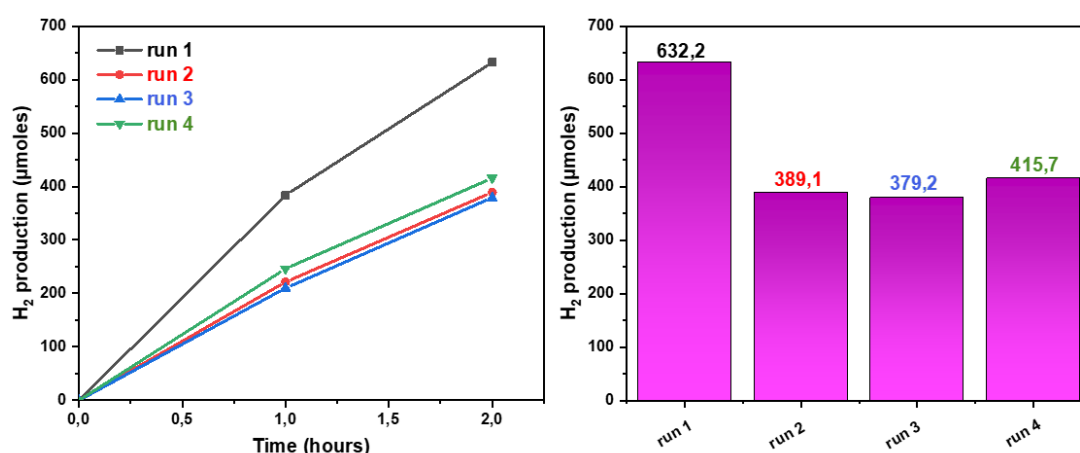


Figure 37: Cycling study of the Pt-decorated catalyst with 0,4wt% Pt. Reaction conditions: 20mg of catalyst, 20mL aqueous solution, 20% v/v of sacrificial agent (TEOA), light irradiation of $\lambda > 360\text{nm}$

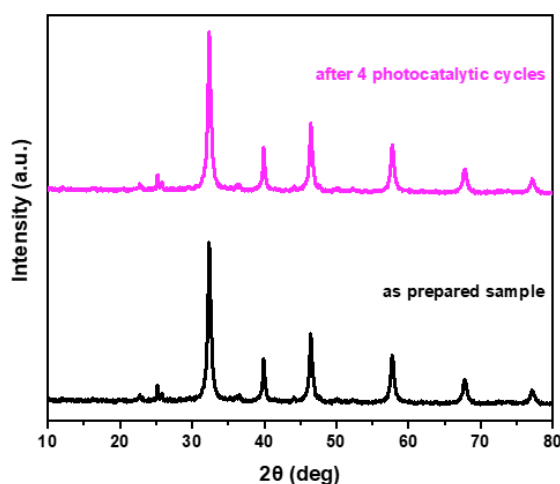


Figure 38: XRD patterns of STO-0,4wt% Pt photocatalyst as prepared and after 4 photocatalytic cycles

Table 6: EDX data of STO-0,4wt% Pt catalyst before and after use

Pt wt% before catalysis	Pt wt% after catalysis
0,4	-

The stability of STO-0,25% Ni catalyst was examined with two photocatalytic cycles, XRD and EDX as well. As seen in **Figure 39** the H₂ production at the second run had a 55,5% decrease. This decrease is justified from the EDX data in **Table 7** where the Ni percentage is decreased too by 40%. The XRD patterns before and after use show no significant change in the catalyst's crystal structure.

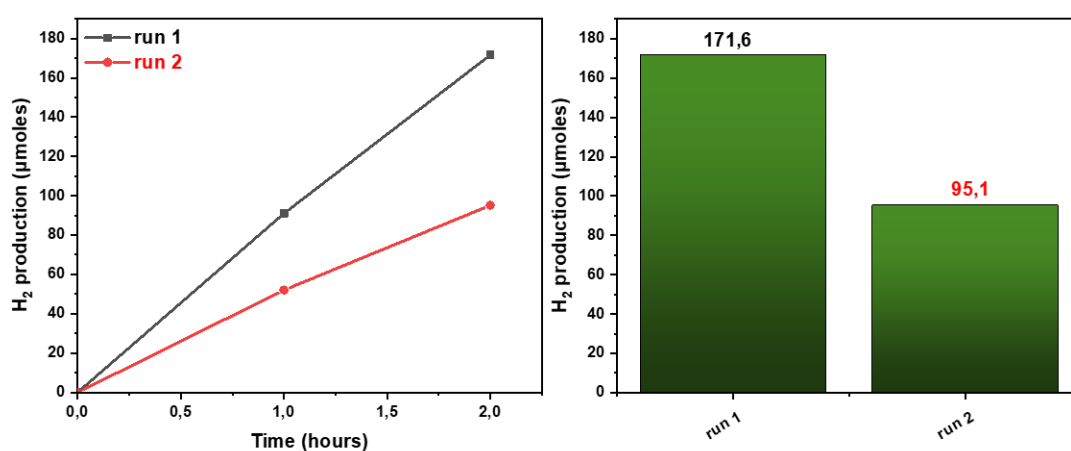


Figure 39: Cycling study of the Ni-decorated catalyst with 0,25wt% Ni. Reaction conditions: 20mg of catalyst, 20mL aqueous solution, 20% v/v of sacrificial agent (TEOA), light irradiation of $\lambda > 360\text{nm}$

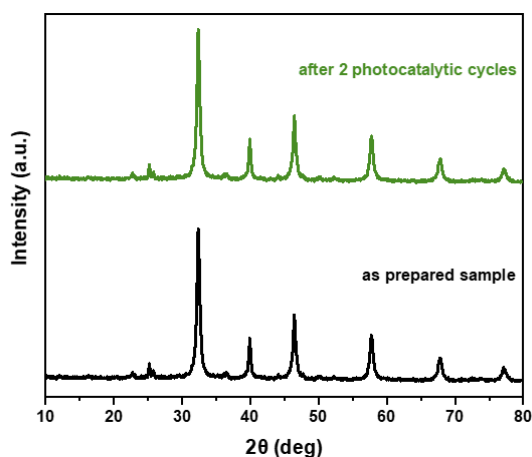


Figure 40: XRD patterns of STO-0,25wt% Ni photocatalyst as prepared and after 2 photocatalytic cycles

Table 7: EDX data of STO-0,25wt% Ni catalyst before and after use

Ni wt% before catalysis	Ni wt% after catalysis
0,25	0,1

The stability of STO-1wt% Cu catalyst was examined as well with, 4 photocatalytic cycles, EDX and XRD similar with the other catalysts. In **Figure 41** four photocatalytic cycles are illustrated. The catalyst STO-1wt% Cu proved to be very stable as it exhibited a slight decrease in its activity of only ~14%. In agreement with this results the EDX data show no significant decrease in the Cu percentage, and the XRD patterns reveal no alteration in the crystal structure.

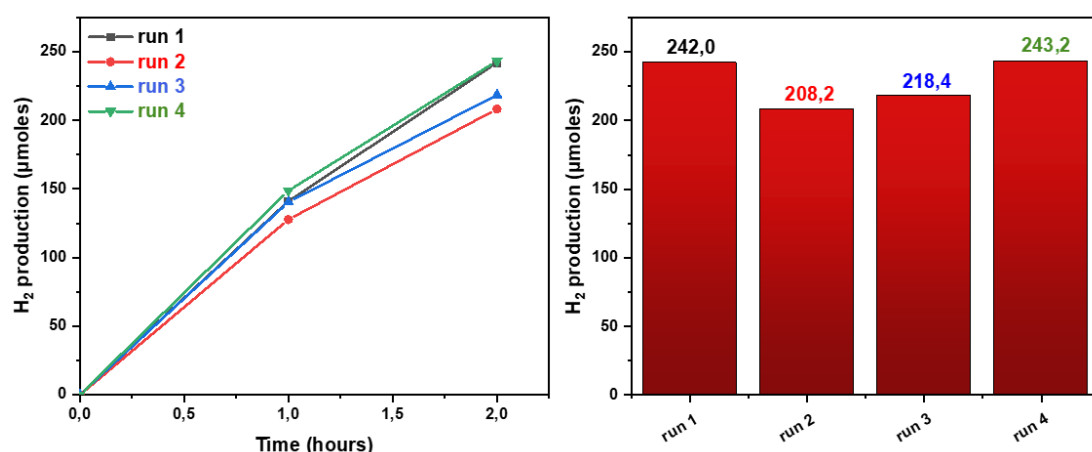


Figure 41: Cycling study of the Cu-decorated catalyst with 1wt% Cu. Reaction conditions: 20mg of catalyst, 20mL aqueous solution, 20% v/v of sacrificial agent (TEOA), light irradiation of $\lambda > 360\text{nm}$

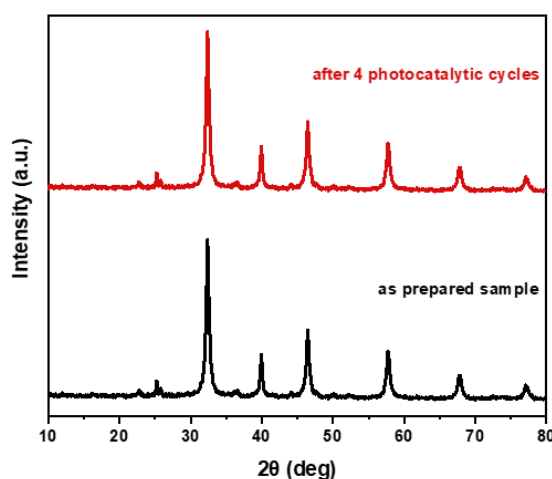


Figure 42: XRD patterns of STO-1wt% Cu photocatalyst as prepared and after 4 photocatalytic cycles

Table 8: EDX data of STO-1wt% Cu catalyst before and after use

Cu wt% before catalysis	Cu wt% after catalysis
1,0	0,97

Chapter 4. Conclusions and perspectives

The purpose of this master thesis was to systematically investigate the effect of metal nanoparticles as co-catalysts on the surface of STO for photocatalytic H₂ production under UV and visible light irradiation. A facile hydrothermal synthetic procedure was followed to synthesis STO and the metal cocatalysts (Pt, Ni and Cu) were loaded on its surface through a simple photodeposition method. XRD pattern of pristine STO showed that it was mixed phased due to peaks of TiO₂ appearing. Additionally, XRD patterns of Pt and Ni loaded STO did not show any peaks attributed to the metals or metal oxides probably due to small loadings. The EDX data of STO-metal series showed agreement with the theoretical and experimental metal loadings. The UV-Vis diffuse reflectance spectra of the samples revealed small shifts of the absorbance spectra of all samples towards higher wavelengths in accordance with pristine STO and the energy gap of the samples was decreasing as the metal loading was increased. SEM and TEM images revealed the morphology of the samples, with pristine STO comprising of small round-shaped nanoparticles varying in diameter from ~20nm-30nm. Also, through TEM images and their analysis the size of Pt nanoparticles was estimated at 2,44nm close to what was expected from literature. As far as the photocatalytic activity of the samples is concerned, the best photocatalytic results were exhibited from STO-0,4wt% Pt, STO-0,25wt% Ni and STO-1wt% Cu with H₂ productions of 632,2μmoles , 171,6μmoles and 138,8μmoles that correspond to x8 times, x2,3 times and x2 times higher production that pristine STO. The photocatalytic experiments done in visible irradiation did not show any significant H₂ production. The most stable catalyst was proven to be STO-1wt% Cu with a slight decrease in the H₂ production of 14% after four cycles, then came the STO-0,4wt% Pt that had a 40% decrease in the second cycle but the activity reached a plateau until the fourth cycle, and finally STO-0,25wt% Ni had a 55% decrease from the second cycle.

Chapter 5. References

- [1] A. Kudo and Y. Miseki, "Heterogeneous photocatalyst materials for water splitting," *Chem. Soc. Rev.*, vol. 38, no. 1, pp. 253–278, 2009, doi: 10.1039/b800489g.
- [2] S. Liu, Z. R. Tang, Y. Sun, J. C. Colmenares, and Y. J. Xu, "One-dimension-based spatially ordered architectures for solar energy conversion," *Chem. Soc. Rev.*, vol. 44, no. 15, pp. 5053–5075, 2015, doi: 10.1039/c4cs00408f.
- [3] Y. Xu and R. Xu, "Nickel-based cocatalysts for photocatalytic hydrogen production," *Appl. Surf. Sci.*, vol. 351, pp. 779–793, 2015, doi: 10.1016/j.apsusc.2015.05.171.
- [4] K. Maeda and K. Domen, "Chapter 12 Nano-particulate photocatalysts for overall water splitting under visible light," *Theor. Comput. Chem.*, vol. 18, pp. 301–315, 2007, doi: 10.1016/S1380-7323(06)80014-2.
- [5] L. Lin, T. Hisatomi, S. Chen, T. Takata, and K. Domen, "Visible-Light-Driven Photocatalytic Water Splitting: Recent Progress and Challenges," *Trends Chem.*, vol. 2, no. 9, pp. 813–824, 2020, doi: 10.1016/j.trechm.2020.06.006.
- [6] S. K. Lakhera, A. Rajan, R. T.P., and N. Bernaurdshaw, "A review on particulate photocatalytic hydrogen production system: Progress made in achieving high energy conversion efficiency and key challenges ahead," *Renew. Sustain. Energy Rev.*, vol. 152, no. April, p. 111694, 2021, doi: 10.1016/j.rser.2021.111694.
- [7] T. Takata *et al.*, "Photocatalytic water splitting with a quantum efficiency of almost unity," *Nature*, vol. 581, no. 7809, pp. 411–414, 2020, doi: 10.1038/s41586-020-2278-9.
- [8] Y. Sakata, T. Hayashi, R. Yasunaga, N. Yanaga, and H. Imamura, "Remarkably high apparent quantum yield of the overall photocatalytic H₂O splitting achieved by utilizing Zn ion added Ga₂O₃ prepared using dilute CaCl₂ solution," *Chem. Commun.*, vol. 51, no. 65, pp. 12935–12938, 2015, doi: 10.1039/c5cc03483c.
- [9] B. Tian *et al.*, "Supported black phosphorus nanosheets as hydrogen-evolving photocatalyst achieving 5.4% energy conversion efficiency at 353 K," *Nat. Commun.*, vol. 9, no. 1, pp. 1–11, 2018, doi: 10.1038/s41467-018-03737-4.
- [10] L. Liao *et al.*, "Efficient solar water-splitting using a nanocrystalline CoO photocatalyst," *Nat. Nanotechnol.*, vol. 9, no. 1, pp. 69–73, 2014, doi: 10.1038/nnano.2013.272.
- [11] L. Finegold and J. L. Cude, "Biological sciences: One and two-dimensional structure of alpha-helix and beta-sheet forms of poly(L-Alanine) shown by specific heat measurements at low temperatures (1.5-20 K)," *Nature*, vol. 238, no. 5358, pp. 38–40, 1972, doi: 10.1038/238038a0.
- [12] J. Yuan, Y. Liu, T. Bo, and W. Zhou, "Activated HER performance of defected single layered TiO₂ nanosheet via transition metal doping," *Int. J. Hydrogen Energy*, vol. 45, no. 4, pp. 2681–2688, 2020, doi: 10.1016/j.ijhydene.2019.11.191.
- [13] Y. Zhu *et al.*, "Red phosphorus decorated and doped TiO₂ nanofibers for efficient photocatalytic hydrogen evolution from pure water," *Appl. Catal. B*

- Environ.*, vol. 255, no. May, 2019, doi: 10.1016/j.apcatb.2019.117764.
- [14] W. Ou *et al.*, “Two-dimensional ultrathin MoS₂-modified black Ti₃+–TiO₂ nanotubes for enhanced photocatalytic water splitting hydrogen production,” *J. Energy Chem.*, vol. 43, pp. 188–194, 2020, doi: 10.1016/j.jechem.2019.08.020.
 - [15] M. A. Bin Adnan, K. Arifin, L. J. Minggu, and M. B. Kassim, “Titanate-based perovskites for photochemical and photoelectrochemical water splitting applications: A review,” *Int. J. Hydrogen Energy*, vol. 43, no. 52, pp. 23209–23220, 2018, doi: 10.1016/j.ijhydene.2018.10.173.
 - [16] Y. Qu, W. Zhou, and H. Fu, “Porous cobalt titanate nanorod: A new candidate for visible light-driven photocatalytic water oxidation,” *ChemCatChem*, vol. 6, no. 1, pp. 265–270, 2014, doi: 10.1002/cctc.201300718.
 - [17] S. K. Lakhera *et al.*, “Enhanced photocatalytic degradation and hydrogen production activity of in situ grown TiO₂ coupled NiTiO₃ nanocomposites,” *Appl. Surf. Sci.*, vol. 449, pp. 790–798, 2018, doi: 10.1016/j.apsusc.2018.02.136.
 - [18] L. Paramanik, S. Sultana, and K. Parida, “ScienceDirect via heterogeneous junction induced benign junction interface for enhanced photocatalytic H₂ evolution,” *Int. J. Hydrogen Energy*, vol. 47, no. 6, pp. 3893–3905, 2021, doi: 10.1016/j.ijhydene.2021.11.047.
 - [19] S. Patial, V. Hasija, P. Raizada, P. Singh, A. A. P. Khan Singh, and A. M. Asiri, “Tunable photocatalytic activity of SrTiO₃ for water splitting: Strategies and future scenario,” *J. Environ. Chem. Eng.*, vol. 8, no. 3, 2020, doi: 10.1016/j.jece.2020.103791.
 - [20] B. L. Phoon, C. W. Lai, J. C. Juan, P. L. Show, and G. T. Pan, “Recent developments of strontium titanate for photocatalytic water splitting application,” *Int. J. Hydrogen Energy*, vol. 44, no. 28, pp. 14316–14340, 2019, doi: 10.1016/j.ijhydene.2019.01.166.
 - [21] X. Shen, T. Kawabata, and K. Sasaki, “Redox-stable Sr_{0.9}La_{0.1}TiO₃-supported SOFC single cells,” *Int. J. Hydrogen Energy*, vol. 42, no. 10, pp. 6941–6949, 2017, doi: 10.1016/j.ijhydene.2016.11.160.
 - [22] G. Chen *et al.*, “Advanced Fuel Cell Based on Perovskite La-SrTiO₃ Semiconductor as the Electrolyte with Superoxide-Ion Conduction,” *ACS Appl. Mater. Interfaces*, vol. 10, no. 39, pp. 33179–33186, 2018, doi: 10.1021/acsami.8b10087.
 - [23] A. M. Dayaghi, K. J. Kim, S. J. Kim, Y. S. Sung, and G. M. Choi, “Oxidation of porous stainless-steel coated with donor-doped SrTiO₃ in anodic atmosphere of solid oxide fuel cell,” *J. Power Sources*, vol. 360, pp. 488–494, 2017, doi: 10.1016/j.jpowsour.2017.06.017.
 - [24] B. H. Park and G. M. Choi, “Effect of anode firing on the performance of lanthanum and nickel co-doped SrTiO₃ (La_{0.2}Sr_{0.8}Ti_{0.9}Ni_{0.1}O_{3-δ}) anode of solid oxide fuel cell,” *J. Power Sources*, vol. 293, pp. 684–691, 2015, doi: 10.1016/j.jpowsour.2015.06.005.
 - [25] X. Shen and K. Sasaki, “Highly redox-resistant solid oxide fuel cell anode materials based on La-doped SrTiO₃ by catalyst impregnation strategy,” *J.*

- Power Sources*, vol. 320, pp. 180–187, 2016, doi: 10.1016/j.jpowsour.2016.04.111.
- [26] X. Lv *et al.*, “Influence of La doping concentration and A-site deficiency on electrical conductivity of La substituted SrTiO₃ and its chemical compatibility with ScSZ,” *Ceram. Int.*, vol. 48, no. 19, pp. 27527–27535, 2022, doi: 10.1016/j.ceramint.2022.06.046.
- [27] P. Cheng *et al.*, “Fiber Bragg grating temperature sensor of cladding with SrTiO₃ thin film by pulsed laser deposition,” *Laser Phys.*, vol. 29, no. 2, 2019, doi: 10.1088/1555-6611/aaf635.
- [28] S. K. Hodak, T. Supasai, A. Wisitsoraat, and J. H. Hodak, “Design of low cost gas sensor based on SrTiO₃ and BaTiO₃ films,” *J. Nanosci. Nanotechnol.*, vol. 10, no. 11, pp. 7236–7238, 2010, doi: 10.1166/jnn.2010.2800.
- [29] A. M. Schultz, T. D. Brown, and P. R. Ohodnicki, “Optical and chemi-resistive sensing in extreme environments: La-doped SrTiO₃ films for hydrogen sensing at high temperatures,” *J. Phys. Chem. C*, vol. 119, no. 11, pp. 6211–6220, 2015, doi: 10.1021/jp512391f.
- [30] J. Xue, C. Gao, L. Zhang, K. Cui, W. He, and J. Yu, “A single-interface photoelectrochemical sensor based on branched TiO₂ nanorods@strontium titanate for the detection of two biomarkers,” *J. Mater. Chem. B*, vol. 6, no. 28, pp. 4697–4703, 2018, doi: 10.1039/c8tb00992a.
- [31] M. Zhang, S. Wei, W. Ren, and R. Wu, “Development of high sensitivity humidity sensor based on gray TiO₂/SrTiO₃ composite,” *Sensors (Switzerland)*, vol. 17, no. 6, pp. 1–6, 2017, doi: 10.3390/s17061310.
- [32] N. Y. Chan *et al.*, “Highly sensitive gas sensor by the LaAlO₃/SrTiO₃ heterostructure with Pd nanoparticle surface modulation,” *Adv. Mater.*, vol. 26, no. 47, pp. 5962–5968, 2014, doi: 10.1002/adma.201401597.
- [33] M. S. Yahya and M. Ismail, “Catalytic effect of SrTiO₃ on the hydrogen storage behaviour of MgH₂,” *J. Energy Chem.*, vol. 28, pp. 46–53, 2019, doi: 10.1016/j.jechem.2017.10.020.
- [34] M. S. Yahya, W. B. Lew, F. A. Halim Yap, and M. Ismail, “The catalytic effect of an inert additive (SrTiO₃) on the hydrogen storage properties of 4MgH₂–Na₃AlH₆,” *Int. J. Hydrogen Energy*, vol. 43, no. 45, pp. 20801–20810, 2018, doi: 10.1016/j.ijhydene.2018.09.086.
- [35] M. S. Yahya and M. Ismail, “Synergistic catalytic effect of SrTiO₃ and Ni on the hydrogen storage properties of MgH₂,” *Int. J. Hydrogen Energy*, vol. 43, no. 12, pp. 6244–6255, 2018, doi: 10.1016/j.ijhydene.2018.02.028.
- [36] W. Gao, M. Yao, and X. Yao, “Achieving Ultrahigh Breakdown Strength and Energy Storage Performance through Periodic Interface Modification in SrTiO₃ Thin Film,” *ACS Appl. Mater. Interfaces*, vol. 10, no. 34, pp. 28745–28753, 2018, doi: 10.1021/acsami.8b07151.
- [37] P. Shi *et al.*, “Large energy storage properties of lead-free (1-x)(0.72Bi_{0.5}Na_{0.5}TiO₃-0.28SrTiO₃)-xBiAlO₃ ceramics at broad temperature range,” *J. Alloys Compd.*, vol. 784, pp. 788–793, 2019, doi:

10.1016/j.jallcom.2019.01.077.

- [38] C. Diao *et al.*, “Structure and electric properties of sandwich-structured SrTiO₃/BiFeO₃ thin films for energy storage applications,” *J. Alloys Compd.*, vol. 781, pp. 378–384, 2019, doi: 10.1016/j.jallcom.2018.11.391.
- [39] H. Pourmohamadian, M. Rahimi-Nasrabadi, G. A. Sheikhzadeh, and H. B. Tabrizi, “Preparation of SrTiO₃-microencapsulated palmitic acid by means of a sol–gel approach as thermal energy storage materials,” *J. Mater. Sci. Mater. Electron.*, vol. 29, no. 1, pp. 794–800, 2018, doi: 10.1007/s10854-017-7974-3.
- [40] H. Bakhshi, R. Sarraf-Mamoory, A. Yourdkhani, A. A. AbdelNabi, and Y. Mozharivskyj, “Sol-gel synthesis, spark plasma sintering, structural characterization, and thermal conductivity measurement of heavily Nb-doped SrTiO₃/TiO₂ nanocomposites,” *Ceram. Int.*, vol. 46, no. 3, pp. 3224–3235, 2020, doi: 10.1016/j.ceramint.2019.10.027.
- [41] S. P. Singh *et al.*, “Thermoelectric properties of A-site deficient La-doped SrTiO₃ at 100–900 °C under reducing conditions,” *J. Eur. Ceram. Soc.*, vol. 40, no. 2, pp. 401–407, 2020, doi: 10.1016/j.jeurceramsoc.2019.09.024.
- [42] D. Srivastava *et al.*, “Anisotropy and enhancement of thermoelectric performance of Sr_{0.8}La_{0.067}Ti_{0.8}Nb_{0.2}O_{3-δ} ceramics by graphene additions,” *J. Mater. Chem. A*, vol. 7, no. 42, pp. 24602–24613, 2019, doi: 10.1039/c9ta02883h.
- [43] C. Wu *et al.*, “The effect of reduced graphene oxide on microstructure and thermoelectric properties of Nb-doped A-site-deficient SrTiO₃ ceramics,” *J. Alloys Compd.*, vol. 786, pp. 884–893, 2019, doi: 10.1016/j.jallcom.2019.01.376.
- [44] X. Yue, J. Zhang, F. Yan, X. Wang, and F. Huang, “A situ hydrothermal synthesis of SrTiO₃/TiO₂ heterostructure nanosheets with exposed (0 0 1) facets for enhancing photocatalytic degradation activity,” *Appl. Surf. Sci.*, vol. 319, no. 1, pp. 68–74, 2014, doi: 10.1016/j.apsusc.2014.07.100.
- [45] I. Atkinson *et al.*, “Influence of preparation method and nitrogen (N) doping on properties and photo-catalytic activity of mesoporous SrTiO₃,” *J. Photochem. Photobiol. A Chem.*, vol. 368, no. September 2018, pp. 41–51, 2019, doi: 10.1016/j.jphotochem.2018.09.019.
- [46] M. Faisal *et al.*, “Polythiophene/mesoporous SrTiO₃ nanocomposites with enhanced photocatalytic activity under visible light,” *Sep. Purif. Technol.*, vol. 190, no. August 2017, pp. 33–44, 2018, doi: 10.1016/j.seppur.2017.08.037.
- [47] S. T. Huang, W. W. Lee, J. L. Chang, W. S. Huang, S. Y. Chou, and C. C. Chen, “Hydrothermal synthesis of SrTiO₃ nanocubes: Characterization, photocatalytic activities, and degradation pathway,” *J. Taiwan Inst. Chem. Eng.*, vol. 45, no. 4, pp. 1927–1936, 2014, doi: 10.1016/j.jtice.2014.02.003.
- [48] D. Yang, Y. Sun, Z. Tong, Y. Nan, and Z. Jiang, “Fabrication of bimodal-pore SrTiO₃ microspheres with excellent photocatalytic performance for Cr(VI) reduction under simulated sunlight,” *J. Hazard. Mater.*, vol. 312, pp. 45–54, 2016, doi: 10.1016/j.jhazmat.2016.03.032.

- [49] D. Yang, X. Zhao, X. Zou, Z. Zhou, and Z. Jiang, "Removing Cr (VI) in water via visible-light photocatalytic reduction over Cr-doped SrTiO₃ nanoplates," *Chemosphere*, vol. 215, pp. 586–595, 2019, doi: 10.1016/j.chemosphere.2018.10.068.
- [50] E. Grabowska, M. Marchelek, T. Klimczuk, W. Lisowski, and A. Zaleska-Medynska, "TiO₂/SrTiO₃ and SrTiO₃ microspheres decorated with Rh, Ru or Pt nanoparticles: Highly UV–vis responsible photoactivity and mechanism," *J. Catal.*, vol. 350, pp. 159–173, 2017, doi: 10.1016/j.jcat.2017.04.005.
- [51] J. Li, F. Wang, L. Meng, M. Han, Y. Guo, and C. Sun, "Controlled synthesis of BiVO₄/SrTiO₃ composite with enhanced sunlight-driven photofunctions for sulfamethoxazole removal," *J. Colloid Interface Sci.*, vol. 485, pp. 116–122, 2017, doi: 10.1016/j.jcis.2016.07.040.
- [52] W. Ji, T. Shen, J. Kong, Z. Rui, and Y. Tong, "Synergistic Performance between Visible-Light Photocatalysis and Thermocatalysis for VOCs Oxidation over Robust Ag/F-Codoped SrTiO₃," *Ind. Eng. Chem. Res.*, vol. 57, no. 38, pp. 12766–12773, 2018, doi: 10.1021/acs.iecr.8b02873.
- [53] J. Kong, Z. Rui, and H. Ji, "Enhanced Photocatalytic Mineralization of Gaseous Toluene over SrTiO₃ by Surface Hydroxylation," *Ind. Eng. Chem. Res.*, vol. 55, no. 46, pp. 11923–11930, 2016, doi: 10.1021/acs.iecr.6b03270.
- [54] C. A. Srtio *et al.*, "Journal of Colloid and Interface Science Photocatalytic overall water splitting without noble-metal : Decorating," *J. Colloid Interface Sci.*, vol. 606, pp. 491–499, 2022, doi: 10.1016/j.jcis.2021.08.049.
- [55] J. W. Liu, G. Chen, Z. H. Li, and Z. G. Zhang, "Electronic structure and visible light photocatalysis water splitting property of chromium-doped SrTiO₃," vol. 179, no. 3, pp. 3704–3708, 2006, doi: 10.1016/j.jssc.2006.08.014.
- [56] L. Wang *et al.*, "ScienceDirect Hydrogen production performance of active Ce / N co-doped SrTiO₃ for photocatalytic water splitting," *Int. J. Hydrogen Energy*, no. xxxx, pp. 1–11, 2022, doi: 10.1016/j.ijhydene.2022.09.076.
- [57] M. A. Elkodous, A. Aatiqah, G. Kawamura, W. Kian, and A. Matsuda, "ScienceDirect Metallic nanoparticles loaded Al e SrTiO₃ supported with RhCr₂ O₃ and CoOOH cocatalysts for overall water splitting," *Int. J. Hydrogen Energy*, vol. 47, no. 85, pp. 36139–36148, 2022, doi: 10.1016/j.ijhydene.2022.08.199.
- [58] M. Kumar, P. Basera, S. Saini, and S. Bhattacharya, "Role of Defects in Photocatalytic Water Splitting: Monodoped vs Codoped SrTiO₃," 2020, doi: 10.1021/acs.jpcc.9b11160.
- [59] T. Puangpetch, T. Sreethawong, S. Yoshikawa, and S. Chavadej, "Hydrogen production from photocatalytic water splitting over mesoporous-assembled SrTiO₃ nanocrystal-based photocatalysts," *J. Mol. Catal. A Chem.*, vol. 312, no. 1–2, pp. 97–106, 2009, doi: 10.1016/j.molcata.2009.07.012.
- [60] I. Tamiolakis *et al.*, "Mesoporous implantable Pt/SrTiO₃:C,N nanocuboids delivering enhanced photocatalytic H₂-production activity via plasmon-induced interfacial electron transfer," *Appl. Catal. B Environ.*, vol. 236, no. March, pp. 338–347, 2018, doi: 10.1016/j.apcatb.2018.05.036.

- [61] E. C. Su, B. S. Huang, and M. Y. Wey, "Enhanced optical and electronic properties of a solar light-responsive photocatalyst for efficient hydrogen evolution by SrTiO₃/TiO₂ nanotube combination," *Sol. Energy*, vol. 134, pp. 52–63, 2016, doi: 10.1016/j.solener.2016.04.007.
- [62] F. Dai, Y. Wang, R. Zhao, X. Zhou, J. Han, and L. Wang, "ScienceDirect enhanced photocatalytic hydrogen performance," *Int. J. Hydrogen Energy*, vol. 45, no. 53, pp. 28783–28791, 2020, doi: 10.1016/j.ijhydene.2020.07.228.
- [63] R. Wang, S. Ni, G. Liu, and X. Xu, "Applied Catalysis B : Environmental Hollow CaTiO₃ cubes modified by La / Cr co-doping for efficient photocatalytic hydrogen production," vol. 225, no. November 2017, pp. 139–147, 2018, doi: 10.1016/j.apcatb.2017.11.061.
- [64] M. Lu, S. Liu, J. Xiong, and W. Li, "Facile coupling CaTiO₃ nanorods with Cu nanoparticles for enhanced photocatalytic hydrogen evolution through efficient charge separation," *Inorg. Chem. Commun.*, vol. 139, no. February, p. 109377, 2022, doi: 10.1016/j.inoche.2022.109377.
- [65] J. Pei *et al.*, "Hierarchical CaTiO₃ nanowire-network architectures for H₂ evolution under visible-light irradiation," *J. Alloys Compd.*, vol. 806, pp. 889–896, 2019, doi: 10.1016/j.jallcom.2019.07.294.
- [66] J. Cai, A. Cao, J. Huang, W. Jin, J. Zhang, and Z. Jiang, "Applied Catalysis B : Environmental Understanding oxygen vacancies in disorder-engineered surface and subsurface of CaTiO₃ nanosheets on photocatalytic hydrogen evolution," *Appl. Catal. B Environ.*, vol. 267, no. November 2019, p. 118378, 2020, doi: 10.1016/j.apcatb.2019.118378.
- [67] T. Soltani, X. Zhu, A. Yamamoto, S. Pratap, and E. Fudo, "Applied Catalysis B : Environmental Effect of transition metal oxide cocatalyst on the photocatalytic activity of Ag loaded CaTiO₃ for CO₂ reduction with water and water splitting," *Appl. Catal. B Environ.*, vol. 286, no. November 2020, p. 119899, 2021, doi: 10.1016/j.apcatb.2021.119899.
- [68] H. Zhao *et al.*, "Transition-Metal-Based Cocatalysts for Photocatalytic Water Splitting," *Small Struct.*, vol. 3, no. 7, p. 2100229, 2022, doi: 10.1002/ssstr.202100229.
- [69] N. Xiao, S. Li, X. Li, L. Ge, Y. Gao, and N. Li, "The roles and mechanism of cocatalysts in photocatalytic water splitting to produce hydrogen," *Chinese J. Catal.*, vol. 41, no. 4, pp. 642–671, 2020, doi: 10.1016/S1872-2067(19)63469-8.
- [70] A. Meng, L. Zhang, B. Cheng, and J. Yu, "Dual Cocatalysts in TiO₂ Photocatalysis," *Adv. Mater.*, vol. 31, no. 30, 2019, doi: 10.1002/adma.201807660.
- [71] K. Wenderich and G. Mul, "Methods, Mechanism, and Applications of Photodeposition in Photocatalysis: A Review," *Chem. Rev.*, vol. 116, no. 23, pp. 14587–14619, 2016, doi: 10.1021/acs.chemrev.6b00327.
- [72] J. Cai *et al.*, "Designed Construction of SrTiO₃/SrSO₄/Pt Heterojunctions with Boosted Photocatalytic H₂ Evolution Activity," *Chem. - A Eur. J.*, vol. 27, no. 25, pp. 7300–7306, 2021, doi: 10.1002/chem.202100101.

- [73] J. Zwara *et al.*, “The effect of imidazolium ionic liquid on the morphology of Pt nanoparticles deposited on the surface of SrTiO₃ and photoactivity of Pt–SrTiO₃ composite in the H₂ generation reaction,” *Int. J. Hydrogen Energy*, vol. 44, no. 48, pp. 26308–26321, 2019, doi: 10.1016/j.ijhydene.2019.08.094.
- [74] M. Zhou *et al.*, “Shape-controlled synthesis of golf-like, star-like, urchin-like and flower-like SrTiO₃ for highly efficient photocatalytic degradation and H₂ production,” *J. Alloys Compd.*, vol. 817, p. 152796, 2020, doi: 10.1016/j.jallcom.2019.152796.
- [75] B. W. Roehrich, R. Han, and F. E. Osterloh, “Hydrogen evolution with fluorescein-sensitized Pt/SrTiO₃ nanocrystal photocatalysts is limited by dye adsorption and regeneration,” *J. Photochem. Photobiol. A Chem.*, vol. 400, no. May, p. 112705, 2020, doi: 10.1016/j.jphotochem.2020.112705.
- [76] T. Kanazawa and K. Maeda, “Light-Induced Synthesis of Heterojunctioned Nanoparticles on a Semiconductor as Durable Cocatalysts for Hydrogen Evolution,” *ACS Appl. Mater. Interfaces*, vol. 8, no. 11, pp. 7165–7172, 2016, doi: 10.1021/acsami.6b00907.
- [77] P. F. Lim *et al.*, “Mechanism insight of dual synergistic effects of plasmonic Pd–SrTiO₃ for enhanced solar energy photocatalysis,” *Appl. Phys. A Mater. Sci. Process.*, vol. 126, no. 7, pp. 1–10, 2020, doi: 10.1007/s00339-020-03739-4.
- [78] S. Wibowo, A. Yamaguchi, S. Shoji, T. Fujita, H. Abe, and M. Miyauchi, “Photo-assisted dry reforming of methane over strontium titanate,” *Chem. Lett.*, vol. 47, no. 7, pp. 935–937, 2018, doi: 10.1246/cl.180347.
- [79] K. Maeda, D. Lu, K. Teramura, and K. Domen, “Simultaneous photodeposition of rhodium-chromium nanoparticles on a semiconductor powder: Structural characterization and application to photocatalytic overall water splitting,” *Energy Environ. Sci.*, vol. 3, no. 4, pp. 471–478, 2010, doi: 10.1039/b915064a.
- [80] K. Maeda, D. Lu, K. Teramura, and K. Domen, “Direct deposition of nanoparticulate rhodium-chromium mixed-oxides on a semiconductor powder by band-gap irradiation,” *J. Mater. Chem.*, vol. 18, no. 30, pp. 3539–3542, 2008, doi: 10.1039/b808484j.
- [81] K. Shao *et al.*, “Modification of Ag nanoparticles on the surface of SrTiO₃ particles and resultant influence on photoreduction of CO₂,” *Appl. Surf. Sci.*, vol. 434, pp. 717–724, 2018, doi: 10.1016/j.apsusc.2017.11.004.
- [82] J. Liu, Y. Sun, Z. Li, S. Li, and J. Zhao, “Photocatalytic hydrogen production from water/methanol solutions over highly ordered Ag–SrTiO₃ nanotube arrays,” *Int. J. Hydrogen Energy*, vol. 36, no. 10, pp. 5811–5816, 2011, doi: 10.1016/j.ijhydene.2011.01.117.
- [83] D. N. Bui, J. Mu, L. Wang, S. Z. Kang, and X. Li, “Preparation of Cu-loaded SrTiO₃ nanoparticles and their photocatalytic activity for hydrogen evolution from methanol aqueous solution,” *Appl. Surf. Sci.*, vol. 274, pp. 328–333, 2013, doi: 10.1016/j.apsusc.2013.03.054.
- [84] B. Wang, S. Shen, and L. Guo, “SrTiO₃ single crystals enclosed with high-indexed {023} facets and {001} facets for photocatalytic hydrogen and oxygen evolution,” *Appl. Catal. B Environ.*, vol. 166–167, pp. 320–326, 2015, doi:

10.1016/j.apcatb.2014.11.032.

- [85] T. Kanazawa, S. Nozawa, D. Lu, and K. Maeda, "Structure and photocatalytic activity of PdCrOx cocatalyst on SrTiO₃ for overall water splitting," *Catalysts*, vol. 9, no. 1, pp. 1–11, 2019, doi: 10.3390/catal9010059.
- [86] C. Hu, H.-X. Huang, and Y.-F. Lin, "Ag-Deposited Electrospun SrTiO₃ Nanofiber with Enhanced Photocatalytic Activity for Degradation of Methylene Orange," *J. Nanosci. Nanotechnol.*, vol. 18, no. 1, pp. 445–450, 2017, doi: 10.1166/jnn.2018.14611.
- [87] X. Zhang *et al.*, "Water oxidation sites located at the interface of Pt / SrTiO₃ for photocatalytic overall water splitting," *Chinese J. Catal.*, vol. 43, no. 8, pp. 2223–2230, 2022, doi: 10.1016/S1872-2067(21)64048-2.
- [88] S. Peng, C. Gan, Y. Yang, S. Ji, and Y. Li, "Low Temperature and Controllable Formation of Oxygen Vacancy SrTiO_{3-x} by Loading Pt for Enhanced Photocatalytic Hydrogen Evolution," *Energy Technol.*, vol. 6, no. 11, pp. 2166–2171, 2018, doi: 10.1002/ente.201800181.
- [89] M. O. Olagunju *et al.*, "Size-Controlled SrTiO₃ Nanoparticles Photodecorated with Pd Cocatalysts for Photocatalytic Organic Dye Degradation," *ACS Appl. Nano Mater.*, vol. 3, no. 5, pp. 4904–4912, 2020, doi: 10.1021/acsanm.0c01086.
- [90] C. Dupas *et al.*, "High permittivity processed SrTiO₃ for metamaterials applications at terahertz frequencies," *Sci. Rep.*, vol. 8, no. 1, pp. 1–8, 2018, doi: 10.1038/s41598-018-33251-y.
- [91] Y. Hikita, Y. Kozuka, T. Susaki, H. Takagi, and H. Y. Hwang, "Characterization of the Schottky barrier in SrRuO₃/Nb: SrTiO₃ junctions," *Appl. Phys. Lett.*, vol. 90, no. 14, pp. 3–6, 2007, doi: 10.1063/1.2719157.
- [92] I. Tamiolakis *et al.*, "Mesoporous implantable Pt/SrTiO₃:C,N nanocuboids delivering enhanced photocatalytic H₂-production activity via plasmon-induced interfacial electron transfer," *Appl. Catal. B Environ.*, vol. 236, no. May, pp. 338–347, 2018, doi: 10.1016/j.apcatb.2018.05.036.
- [93] H. B. Michaelson, "The work function of the elements and its periodicity," *J. Appl. Phys.*, vol. 48, no. 11, pp. 4729–4733, 1977, doi: 10.1063/1.323539.
- [94] Y. Shiraishi, H. Sakamoto, Y. Sugano, S. Ichikawa, and T. Hirai, "Pt-Cu bimetallic alloy nanoparticles supported on anatase TiO₂: Highly active catalysts for aerobic oxidation driven by visible light," *ACS Nano*, vol. 7, no. 10, pp. 9287–9297, 2013, doi: 10.1021/nm403954p.
- [95] I. Vamvasakis, B. Liu, and G. S. Armatas, "Size Effects of Platinum Nanoparticles in the Photocatalytic Hydrogen Production Over 3D Mesoporous Networks of CdS and Pt Nanojunctions," *Adv. Funct. Mater.*, vol. 26, no. 44, pp. 8062–8071, 2016, doi: 10.1002/adfm.201603292.
- [96] I. Vamvasakis *et al.*, "Visible-Light Photocatalytic H₂ Production Activity of β -Ni(OH)₂-Modified CdS Mesoporous Nanoheterojunction Networks," *ACS Catal.*, vol. 8, no. 9, pp. 8726–8738, 2018, doi: 10.1021/acscatal.8b01830.

